DISCLAIMER

ORNL/SPR-2025/4014

Feature Based Qualification of 17-4PH Stainless Steel to Evaluate Location-Specific Variability in Wire Arc Additive Manufacturing

Pavan Ajjarapu
Yukinori Yamamoto
William Carter
Andrzej Nycz
Wen Dong
Yousub Lee
Zackary Snow
Jeffrey Burdick
Soumya Nag

July 2025

OAK RIDGE National Laboratory

ORNL IS MANAGED BY UT-BATTELLE LLC FOR THE US DEPARTMENT OF ENERGY

ORNL/SPR-2025/4014

Materials Science and Technology Division
Oak Ridge National Laboratory

FEATURE BASED QUALIFICATION OF 17-4PH STAINLESS STEEL GEOMETRIES TO EVALUATE LOCATION-SPECIFIC VARIABILITY IN WIRE ARC ADDITIVE MANUFACTURING

Pavan Ajjarapu
Yukinori Yamamoto
William Carter
Andrzej Nycz
Wen Dong
Yousub Lee
Zackary Snow
Jeffrey Burdick
Soumya Nag

July 2025

Prepared by
OAK RIDGE NATIONAL LABORATORY
Oak Ridge, TN 37831
managed by
UT-BATTELLE LLC
for the
US DEPARTMENT OF ENERGY
under contract DE-AC05-00OR22725

LIST OF FIGURES

LIST OF TABLES

CONTENTS

ABSTRACT

Qualifying large-scale metal additive manufacturing (M-AM) technologies such as wire arc additive manufacturing (WAAM) can be challenging. This is especially significant in precipitation hardened martensitic stainless steels like SS 17-4PH, where thermal histories induce location-specific microstructural variability and property inhomogeneity/anisotropy. The Department of Defense (DOD) and the United States Army Combat Capabilities Development Command Ground Vehicle Systems Center (GVSC) Ground Vehicle Materials Engineering (GVME) aim to build robust and qualified large-scale M-AM workflows that could reduce the time and cost through quick and informed evaluation, testing, and development of feedstock, processes, and parts. The report presents the findings from the first phase of a multi-phase collaborative efforts between Oak Ridge National Laboratory (ORNL) and the U.S. Army GVSC GVME. The aim of this project was to develop a geometric feature-based qualification framework for WAAM of SS 17-4PH components. This report outlines selection methodology of representative build geometries, optimization of WAAM process parameters, in-situ monitoring, microstructure-property evaluation, thermal simulations, as well as data visualization techniques incorporated in this project. The results from this project demonstrate a clear understanding of thermal history dependent phase evolution and consequent location-specific property variations in WAAM of SS 17-4PH. These results in conjunction with the data-driven methodologies used in this project are expected to reduce qualification timelines, improve predictability, and accelerate the development of reliable feature-based qualification strategies for part production via large-scale M-AM technologies.

1. INTRODUCTION

Metal additive manufacturing (M-AM) technologies have changed the way complex metal parts are fabricated at large-scale, especially in critical applications such as aerospace, defense, and energy [4, 5]. M-AM technologies use a layer-by-layer and track-by-track approach that make it easier to make complex near-net-shaped (NNS) structures. This results in a significant reduction in both time and cost [6-11]. On a broad level M-AM can be categorized based on the type of feedstock (wire or powder), feedstock feeding mechanism (powder bed or blown powder), and the heat source (laser, electron beam, or electric arc)[12]. Wire arc additive manufacturing (WAAM) is one such M-AM technique that has been getting a lot of attention due to its ability to make large-scale metal components [7, 8, 13-18]. WAAM offers high deposition rates, cheap feedstock alternatives, and works well with existing welding equipment. In this technique, wire is used as feedstock material and is heated using an electric arc, to create a melt pool that is deposited layer-by-layer [7, 19, 20]. Unlike traditional manufacturing methods, WAAM can make medium- to large-sized parts with high deposition rates, which translates to lesser material waste.

Past researchers demonstrated the ability to process different material systems such as titanium-based [21, 22], aluminum-based [14, 23], steel-based [6, 7, 16-18, 24], and nickel-based alloys [25] using M-AM technology. Stainless steels, which include austenitic, martensitic, and duplex types, have excellent mechanical qualities and strong resistance to corrosion making it a suitable choice for WAAM [11, 16, 26, 27]. 17-4PH stainless steel (SS 17-4PH) is one such material system that has proven to be suitable for additive manufacturing due to its strength, corrosion resistance, and weldability.

SS 17-4PH is a type of martensitic precipitation-hardened stainless steel that finds applications in many industries, such as aerospace, defense, nuclear power generation, and oil and gas [17, 28]. Martensitic phase transformation and nano-scale copper precipitation in the entire matrix are the main hardening mechanisms in SS 17-4PH. There is extensive research on fusion welding of SS 17-4PH alloy to date. However, in spite of the process similarities between fusion welding and WAAM, only a limited number of research papers in WAAM of SS 17-4PH material system are currently available. **Table 1** outlines the mechanical property results observed in available literature, for WAAM of SS 17-4PH along with a few recent publications on laser powder bed fusion (LPBF) and directed energy deposition (DED) of SS 17-4PH to highlight the spread in mechanical properties of M-AM processed SS17-4PH in their as-printed condition [6, 17, 29].

Table 1: Mechanical properties of as-printed SS 17-4PH alloy fabricated via WAAM, LPBF, and BP-DED modalities based on data from past literature

Reference	Year	AM Modality	Mechanical Properties			
			Hardness (HV)	Yield Strength (MPa)	UTS (MPa)	% Elongation
[6]	2019	WAAM	320-340	708-907	966-1064	11.3 – 12.9
[30]	2022	WAAM	325-350	678 ± 3	975 ± 16	11.7 ± 0.1
[31]	2023	WAAM	326-370	N/M	1028-1153	12.3 – 18.5
[32]	2024	WAAM	315-360	636-698	1150-1187	7.2 - 12.5
[33]	2021	LPBF	300-350	520	1150	8
[34]	2022	LPBF	358-365	N/M	N/M	N/A
[35]	2019	LPBF	N/M	830	887	N/A
[36]	2024	LPBF	426 ± 16	1218 ± 68	1431 ± 5	10 ± 1
[37]	2020	BP-DED	402	N/M	N/M	N/M
[38]	2023	BP-DED	360	937	1008	8
[32]	2024	Wrought	N/M	725	954	>20

It is to be noted SS 17-4PH as a material system is highly sensitive to temperature, and that thermal history has a big effect on the microstructures of WAAM stainless steel [36-39]. WAAM process includes many cycles of heating and cooling making the thermal history as any given location in the build complicated, leading to the deposited components to have non-equilibrium microstructures [36]. To understand the thermal history of the component, it is important to understand the interdependency of geometrical features and path planning strategies on location-specific temperature profiles. Optimal deposition path planning can greatly lower residual stresses [40]. A lot of research has focused on welding paths that involve thin-walled structures and simple shapes [41-44] . However, there is not enough knowledge of how changes in geometry affect the performance of both thin and thick walls, especially in bigger parts. Therefore, it is important to optimize WAAM deposition strategies, understand thermal history, and identify how heat input, cooling rate, and reheating affect the shape, microstructure, and mechanical properties of WAAM parts. The authors acknowledge that this material system (SS 17-4PH) is not commonly used in its as-built condition and is often heat treated. However, it is quintessential to have a systematic understanding of the effect of build parameters and geometric shape to identify the path function that causes variability (if any) in post-heat-treated samples.

An other key challenge with M-AM technologies (especially at large-scale) is irregularities in process dependability that make it hard for more businesses to adopt these techniques for full-scale manufacturing [19]. To make M-AM part production more efficient, it is important to fully understand and describe the quality of an additively manufactured part while eliminating the need for trial and error. For decades, researchers have used benchmark test artifacts from different additive printing methods to check feasibility of a process is and quality of the parts printed at given process parameters [47-55].

In the more recent past, researchers focused on using empirical models, statistical methods, and advanced machine learning and deep learning techniques to approach and address M-AM challenges [56-58]. While conventional M-AM qualification relies heavily on trial-and-error testing of full-scale components, it can become expensive, slow, and also fail to capture local variability inherent in WAAM processes. Thermal gradients in WAAM can introduce location-specific changes in microstructure and properties. To address these challenges in large-scale manufacturing of complex components using WAAM, Oak Ridge National Lab (ORNL) and United States Army Combat Capabilities Development Command Ground Vehicle Systems Center (GVSC) Ground Vehicle Materials Engineering (GVME) collaborated towards developing feature-based qualification strategy that emphasizes the construction and analysis of simplified geometric features. The goal of these features' designs is to capture the thermal, structural, and dimensional complexities that are common in real-world components. Understanding geometry-dependent and process dependent microstructure-property variations in these features will help speed up the property-structure-processing (PSP) mapping and validation procedures, thereby accelerating reliable part production timelines.

This report is a concatenation of the results and learning from this collaboration between ORNL and the US Army GVSC-GVME. Section 2 of this report outlines the objectives set out for this project. Subsequently, Section 3 discusses the methodology and devise deeper into the first few objectives of this project, discussing the state-of-the-art literature, brainstorming session with stakeholders to down-select test geometries, WAAM process parameters used for this study, and in-situ monitoring techniques implemented. Section 4 presents the microstructure and mechanical property results observed from experiments conducted on the test geometries, as well as thermal simulation results. Section 5 delves deeper into discussing the PSP relationships that define the results observed, and its implications for thermal history dependency on microstructure-property variations in WAAM of SS 17-4PH. Additionally, Section 5 also discusses the significance of data monitoring in WAAM and introduces the use of data visualization platform used in this project. Finally, this report concludes with Section 6 summarizing the key findings from this study, their implications, and its broader impact on future developments in the field of feature-based qualification methodologies for large-scale metal additive manufacturing.

2. PROJECT OBJECTIVES

With a vision to build a robust and efficient workflow for fabricating large-scale components using WAAM, the overarching goal of this project was to create a scalable, data-driven feature-based qualification framework for WAAM of SS 17-4PH. The objectives are broadly classified as follows:

- Conduct a comprehensive literature review of WAAM for SS 17-4PH
- Collaborate with stakeholders to define and down-select test geometries
- Establish baseline WAAM process parameters
- Monitor in-situ thermal conditions
- Characterize microstructures and mechanical performance
- Simulate thermal profiles to validate microstructure-property variations
- Correlate property-structure-processing (PSP) relationships to discuss phase evolution and consequent location-specific property variations
- Demonstrate data-monitoring significance through data visualization platform developed in-house at ORNL-MDF

3. METHODOLOGY

3.1 LITERATURE REVIEW

To establish the scientific foundation for pursuing a feature-based qualification framework in WAAM of SS 17-4PH, a comprehensive review of state-of-the-art research literature was conducted with references to over 150 research articles [59]. The literature review not only helps putting the most recent developments in WAAM of SS 17-4PH in context but also identified challenges with processing and qualification of large-scale components using WAAM. The review outlined several fundamentals from research literature including - solidification behavior of SS 17-4PH under non-equilibrium thermal cycles, phase transformations during solidification, role of thermal gradients in microstructure heterogeneity of welded SS 17-4PH, and precipitation of Cu-rich phases resulting in hardness and mechanical property variations.

This review indicates the focus of past research on bulk properties and coupon-level testing of as-printed and heat-treated SS 17-4PH while highlighting a clear dearth in understanding the influence of complex geometric features on localized microstructural evolution and mechanical behavior [59]. While past researchers studied the sensitivity of SS 17-4PH to process parameters such as heat input, inter-pass temperature, and cooling rate, the effect of spatial variations in thermal histories as a function of part geometry was seen to be neglected [59]. This leaves a huge void in understanding how geometric discontinuities—such as overhangs, thin walls, fillets, and intersections—affect thermal cycling, phase transformations, and consequent performance-critical properties like tensile strength, impact toughness and fatigue resistance. The literature review also revealed the lack of systematic methodologies to correlate localized thermal conditions with microstructural variations and property outcomes across complex part geometries. These limitations underscored the need for an overarching geometric feature-driven approach to qualification—particularly for application-based and mission-critical large-scale components fabricated via WAAM.

This project is geared towards directly addressing such gaps in the literature by implementing a feature-based investigation of representative geometries, capturing in-situ thermal data and correlating it with spatially resolved microstructure and mechanical property analysis. The results from this project will build on the existing literature and expand the knowledge-base by offering a first-of-its-kind pathway towards location-specific qualification protocols that better reflect the realities of large-scale WAAM part performance.

3.2 BRAINSTORMING SESSION FOR FEATURE SELECTION

To ensure the relevance, applicability, and necessity of a feature-based qualification (FBQ) framework for WAAM of SS 17-4PH, a focused brainstorming session was convened with key stakeholders from government, academia, and the industry. The session was attended by 14 experts from 7 different organizations - the U.S. Army Ground Vehicle Systems Center (GVSC), Oak Ridge National Laboratory (ORNL), National Institute for Aviation Research (NIAR), Edison Welding Institute (EWI), Naval Surface Warfare Center (NSWC) Carderock, University of Michigan, and Michigan Technological University.

The primary goal of this session was to collaboratively identify and narrow down geometric features from potential real-world components that have metallurgical and thermal significance, in the context of WAAM technology. Participants of this session proposed multiple geometric features of interest including vertical walls, overhangs, thin fins, thick-to-thin transitions, fillets, internal channels, and corner junctions. **Figure 1** shows some of the geometries that were deliberated upon by the participants of this brainstorming session. Proposed features were discussed based on their functional significance, frequency of the feature's occurrence in mission-critical components, and more importantly – the uniqueness of the feature in the context of processing and thermal histories.

Vertical walls for example, were accepted to be a recurring feature in most application-based components. These geometries often exhibit rapid heat dissipation and high surface-area-to-volume ratios, and potential heat accumulation in thicker walls, making them susceptible to anisotropy in microstructure and mechanical properties. Similarly, overhangs and cantilevers were highlighted for their relevance to unsupported features and brackets with complex deposition strategies and cooling rate variabilities. Internal channels for fluid and cooling applications were considered from a performance design perspective. However, fabrication feasibility – especially by WAAM was debated. Fillets and sharp corners were invoked as metallurgically interesting features with the potential to act as stress concentrators during failure. Finally, the group concluded the discussions with proposed interest in thick-to-thin transitions that are prevalent in load-bearing hubs, lugs, and structural joints. These transitions are known to be highly sensitive to deposition strategies, often resulting in local hardness variations, residual stresses, and microstructural heterogeneity based on cooling rates and heat accumulation.

After considering the technical relevance, processing complexities, and characterization strategies for each geometry, a phased approach was proposed. It was determined that this project would commence with a subset of simple yet highly informative features that can establish clear processing-structure-property (PSP) relationships under controlled conditions before tackling complex, multi-featured components.

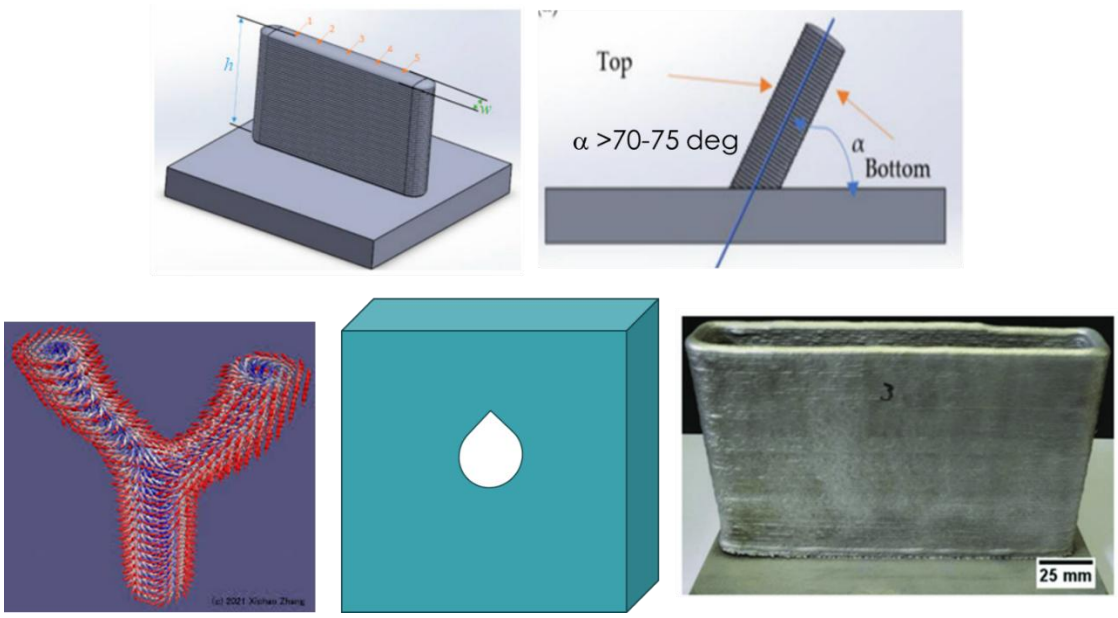

Figure 1: Schematics of proposed feature geometries inspired from past literature [1-3]

3.3 WAAM PROCESS PARAMETERS AND FEATURE DEPOSITION

The design freedom, high deposition rates, and ability to fabricate large-scale components gives WAAM an edge over other M-AM techniques. However, it is still important for the parts fabricated using WAAM to be defect-free and comparable with other M-AM components in terms of physical, mechanical, and chemical properties. Macroscopic flaws such as porosity and weld spatter are known to be very sensitive to process parameters including wire feeding speed, scanning speed, welding current mode, cooling time, and interlay temperature [5, 7, 9, 14, 60]. Moreover, thermal history of the processes was found to have a significant impact on the microstructures of WAAM stainless steel [39-41]. Some of the most common problems found in stainless steel parts made with WAAM are porosity (which shows up as cracks, keyholes, lack of fusion, and gas porosity), undercutting, residual stresses, non-homogeneity in microstructure, formation of brittle phases, and anisotropic characteristics [61]. To determine optimum process parameters for the down-selected geometric features, and to ensure printability of defect-free parts, ORNL typically employs a process parameter development strategy that uses a stable arc to deposit single beads as shown in **Figure 2**. The wire feed speed is slowly ramped up while adjusting the trim and move speed while continuing to tune parameters during the single-bead builds. This is followed by deposition of multi-bead walls to measure and compare layer height and bead spacing before finalizing on the optimal print parameters.

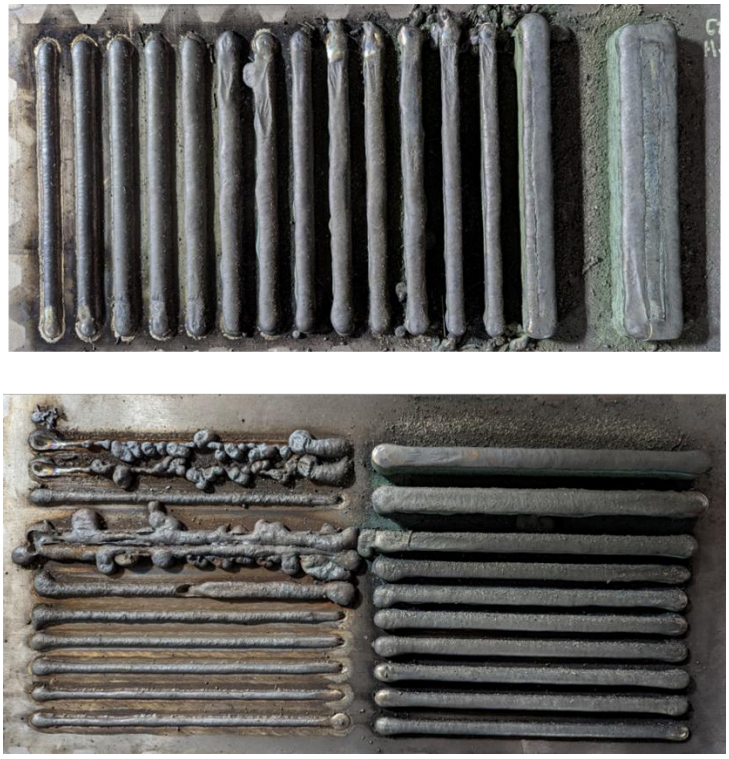

Figure 2: Single bead depositions for process parameter development

All the WAAM builds in this project were deposited using Lincoln Electric's Arc Cell at ORNL's Manufacturing Demonstration Facility (ORNL-MDF) with standardized parameters from the parameter development exercise performed on a similar material system in the past. The process parameters used for this project as listed in **Table 2** and have been kept constant across all the geometric features deposited for the purpose of this project.

Table 2: Process parameters used for all the geometric features deposited in this study

Shielding gas	80% Ar + 20% He
Weld speed	40 in/min (16.9 mm/s)
Weave length	0.12 in (3 mm)
Weave width	0.008 in (0.2 mm)
Weld mode	503 – Pulse
Trim	0.7
Wire feed	400 in/min (169.3 mm/s)
Ultimarc	0
Average Voltage	205V
Interpass Temp	400°C (752°F)

Following-up on the insights from the brainstorming session, ORNL and U.S. Army GVSC GVME narrowed down the work scope of this project to 4 simple geometric features (as shown in **Figure 3**):

1. Thin vertical walls of 2-bead (2B), 4-bead (4B), and 8-beads (8B) – 200 mm long and 200 mm tall.

2. Thin inclined walls of 2-bead (2B), 4-bead (2B), and 8-beads (2B) – 200 mm long and 200 mm tall.

3. Thick vertical wall of 20-beads (20B) - 200 mm long and 200 mm tall.

4. A stair-step (or) wedge feature with varying beads along the length of the part

The 20-Bead thick (20B) wall is designed to understand the key differences not only across the height, but also across the width of the wall. Whereas the wedge feature is designed to understand thick-to-thin transition zone where effective heat input at any given location is the same, owing to toolpath strategy. These down-selected features represent a balance between experimental feasibility and industrial relevance while enabling targeted investigation of thermal gradients, microstructure evolution, and mechanical response by providing scientific insights on feature-based variations.

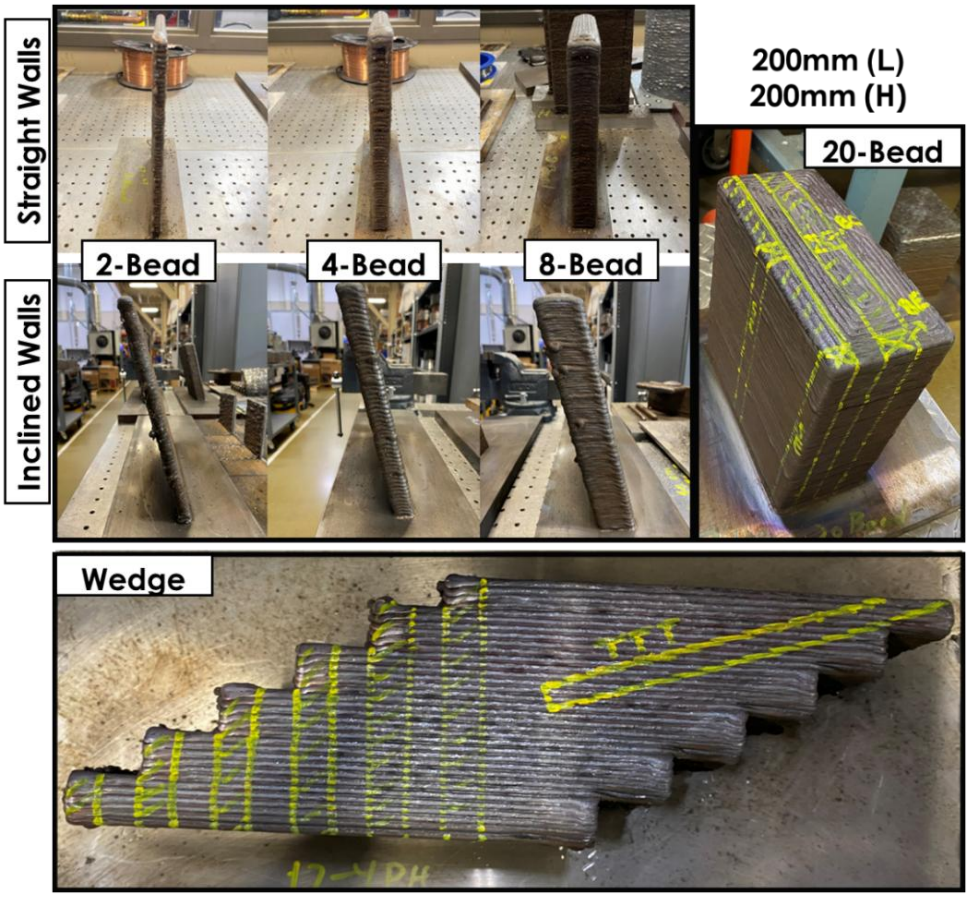

Figure 3: A collage summarizing all the geometric features deposited in this study

3.4 SAMPLE EXTRACTION STRATEGY FOR METALLOGRAPHY AND MECHANICAL TESTING

To enable spatial characterization of WAAM SS 17-4PH, a systematic sample extraction strategy was implemented. Particularly for metallographic analysis of the straight walls and inclined walls of 2-bead, 4-bead, and 8-bead thicknesses, samples were extracted from the top, middle, and bottom of the walls, at the center and at the edge of the walls respectively as shown in **Figure 4**. The 20-bead thick wall was sectioned into thinner sections at the bulk and at the surface to understand spatial variation in microstructure and properties along the transverse direction (thickness) of the wall. Samples from top, middle, and bottom were extracted from bulk-center (BC), bulk-edge (BE), surface-center (SC), and surface-edge (SE) of the 20-bead wall. For the stir-stepped wedge feature on the other hand, samples were extracted from the single stepped (W1), and from the center and edge of 6-stepped (W6-C and W6-E). Metallographic samples obtained were mounted, grinded, and polished for EBSD quality and used for optical microscopy, Final polishing was performed on a vibratory polisher using colloidal silica solution for 6 h. Vicker's hardness measurements, Scanning Electron Microscopy (SEM), and electron back scattered diffraction (EBSD) analysis.

Remnants from the 2B, 4B, 8B straight and inclined walls, as well as from the bulk and center of the 20B walls were sent out for tensile and Charpy V-notch testing. Tensile samples from the 2B, 4B, and 8B straight walls were extracted from the top, middle and bottom in horizontal. Vertical, and at a 45-degree angle with respect to the build direction. For the inclined walls and the 20B thick wall however, tensile samples were extracted in the horizontal and vertical directions from the middle of the walls. 0.2% Yield strength, ultimate tensile strength (UTS), and % Elongation were recorded and compared. Miniaturized tensile specimens (0.640" length and 0.160" diameter) were machined and tested according to ASTM E8 standards. Charpy V-notch samples were extracted from the longitudinal and transverse directions for all the builds and tested in accordance to ASTM E23 standard. V-notches were oriented perpendicular to the build direction enabling evaluation of fracture energy absorption in relation to thermal histories and microstructural features.

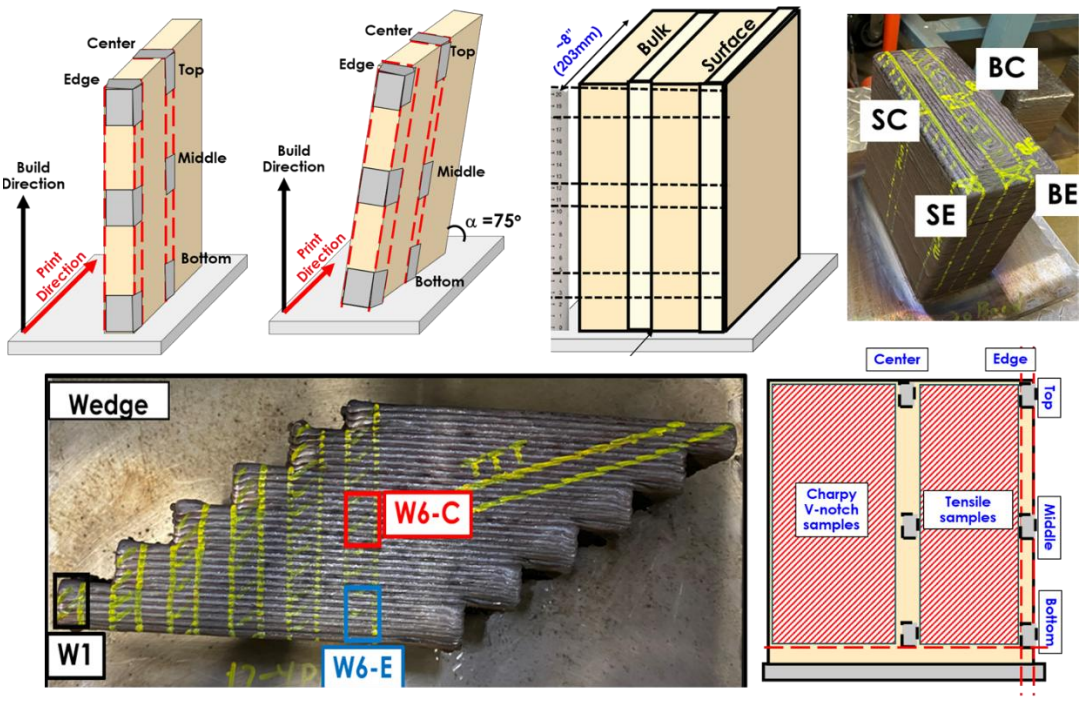

Figure 4: Cut strategy implemented for extracting samples for metallography and mechanical testing in each geometric feature

4. EXPERIMENTAL RESULTS

4.1 MICROSTRUCTURE CHARACTERIZATION

Microstructural characterization was performed using optical microscopy (OM) and electron backscatter diffraction (EBSD) analysis on a scanning electron microscope (SEM) to identify grain morphology, grain crystallographic orientation, and phase distribution across the range of WAAM SS 17-4PH geometries. Optical micrographs of polished and etched cross-sections for the straight walls, inclined walls, and the 20-bead thick wall are shown in **Figure 5**, **Figure 6**, and **Figure 7** respectively. Most of the observed microstructure consisted of a predominantly dendritic prior austenite grain structure which were filled with martensitic laths. Directionally solidified columnar grains oriented at an angle to the build direction are considered being attributed to the steep thermal gradients across the melt pool boundaries during deposition.

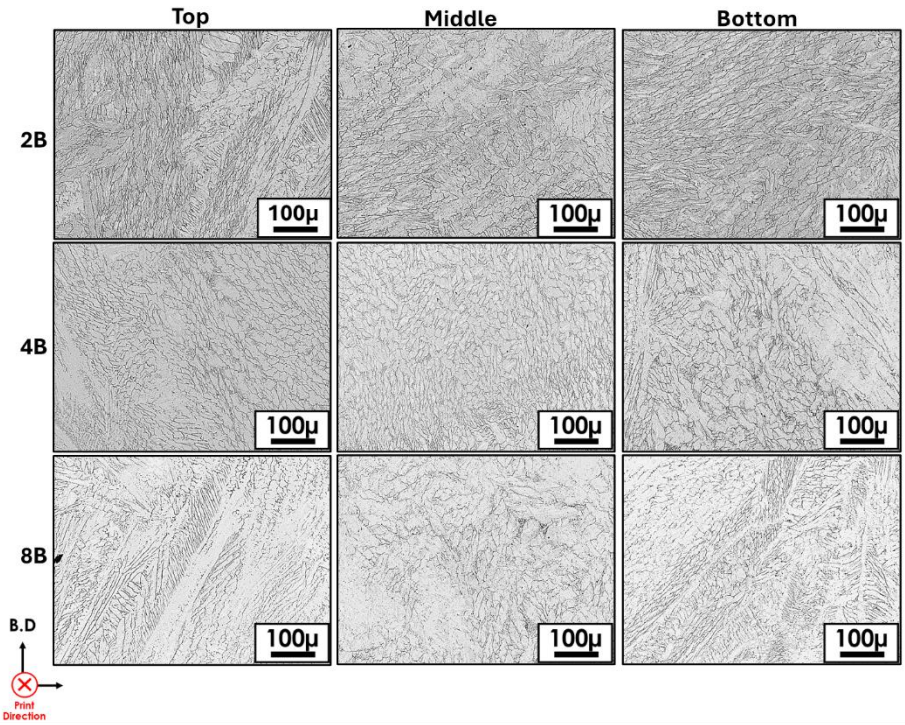

Figure 5: Optical micrographs of samples from the top, middle, and bottom regions of 2-bead, 4-bead, and 8-bead straight walls

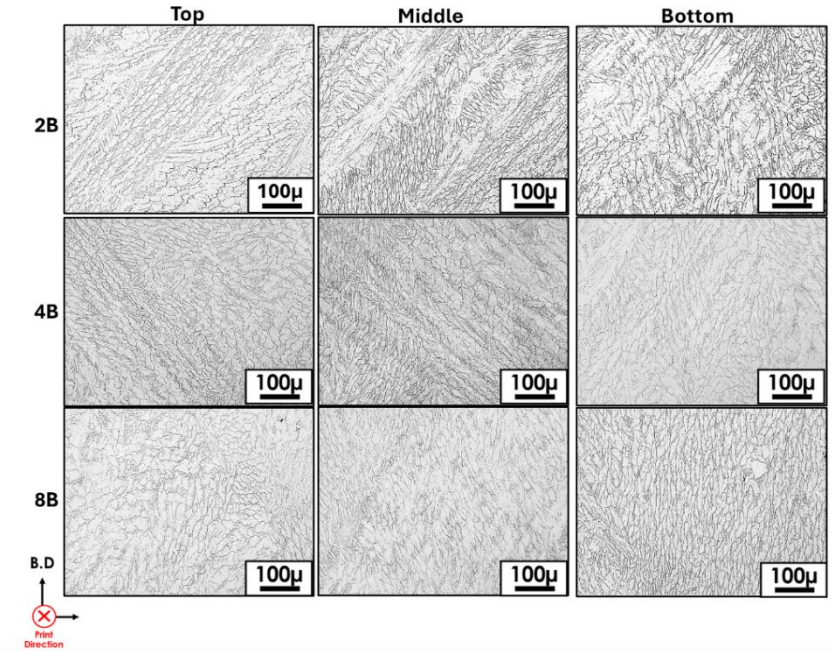

Figure 6: Optical micrographs of samples from the top, middle, and bottom regions of 2-bead, 4-bead, and 8-bead inclined walls

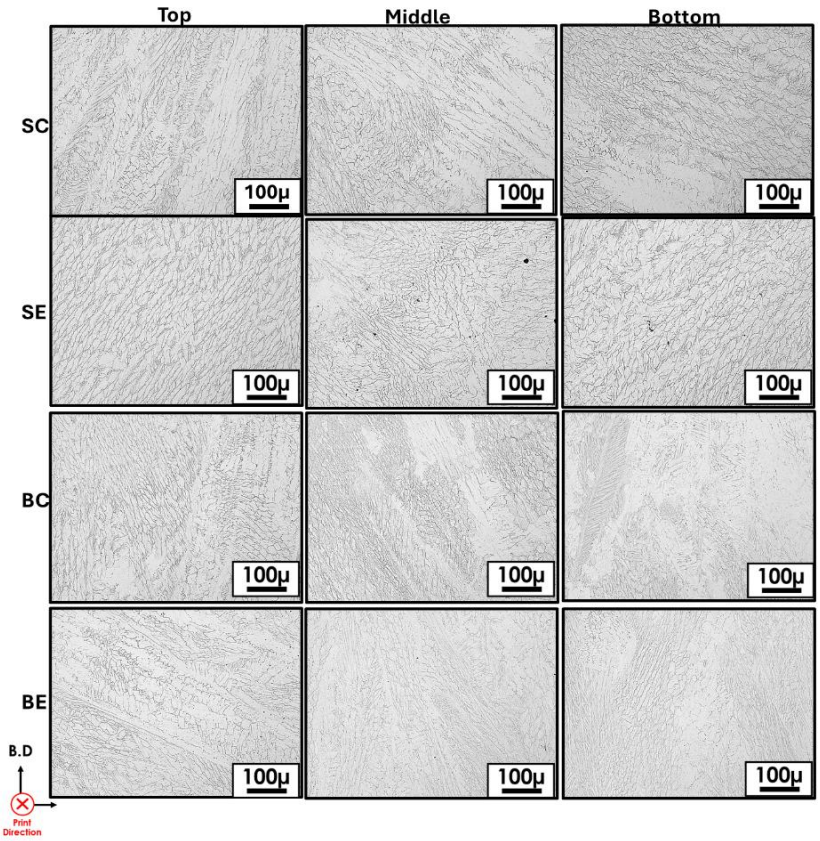

Figure 7: Optical micrographs of samples from the top, middle, and bottom regions of the 20-bead thick wall from surface center (SC), surface edge (SE), bulk center (BC), and bulk edge (BE) respectively

SEM-EBSD analysis was used to evaluate crystallographic orientation, grin size, grain aspect ratio, Kernel Average Misorientation (KAM), and phase content. Martensite is a metastable non-equilibrium phase formed once the high-temperature austenite matrix is supercooled below Ms temperature at arournd ~134°C though continuous cooling process, resulting in a supersaturated solid solution with a body-centered tetragonal (BCT) structure in which the solute carbon atoms are frozen inside the iron lattice due diffusion-less phase transformation. A unit cell rotated at 45° angle along <001> direction of the parent FCC austenite results in the unit cell of BCT martensite, which is known as Bain correspondence of martensite [62]. Further, the crystallographic orientation between the parent austenite and low carbon martensite can be described by Kurdjumov-Sachs (KS) relationship [63-65]. **Figure 8**, **Figure 9**, **Figure 10**, and **Figure 11** show inverse pole figure (IPF) maps of samples extracted from straight walls, inclined walls, 20B thick wall, and the stair-stepped wedge geometry, respectively. Across all sampled geometries, EBSD maps showed a predominantly martensitic BCC phase outlined by high angle grain boundaries.

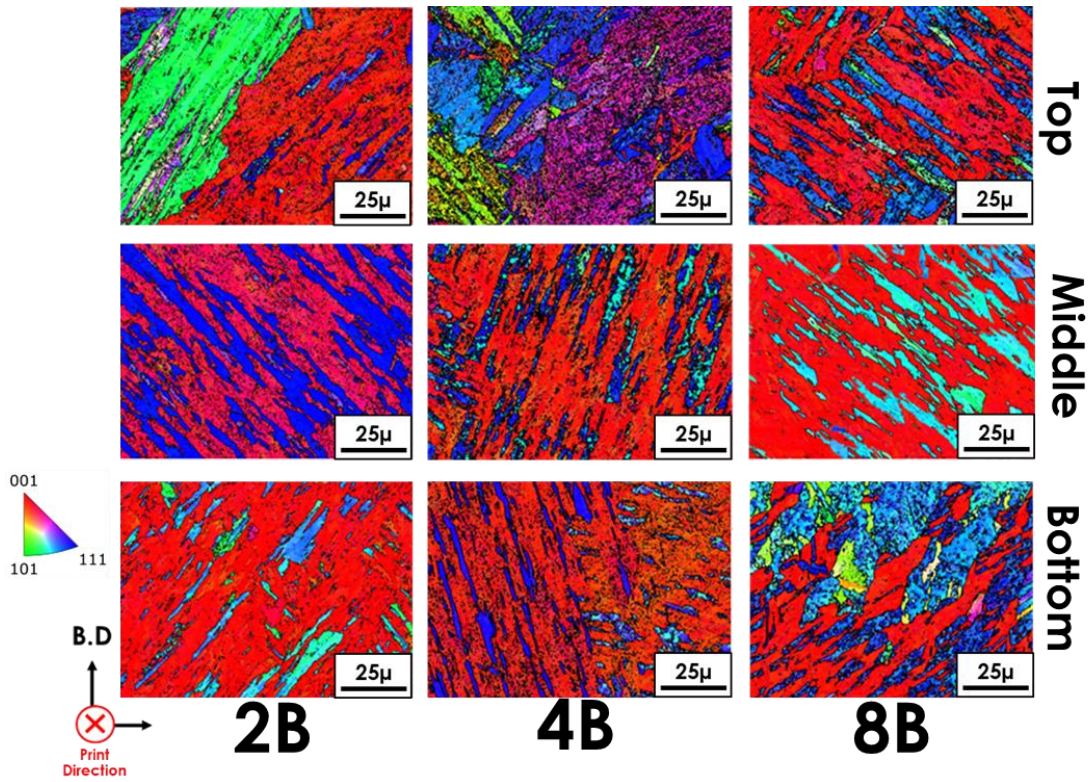

Figure 8: Inverse pole figure map of samples from the top, middle, and bottom regions of 2-bead, 4-bead, and 8-bead straight walls

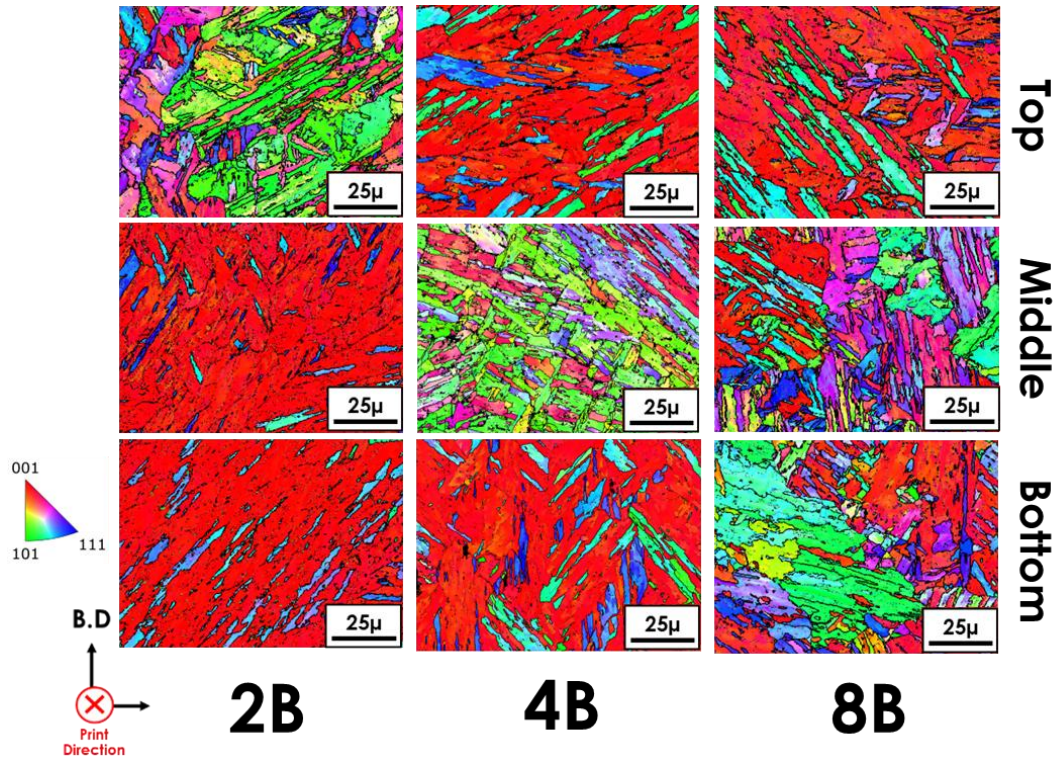

Figure 9: Inverse pole figure map of samples from the top, middle, and bottom regions of 2-bead, 4-bead, and 8-bead inclined walls

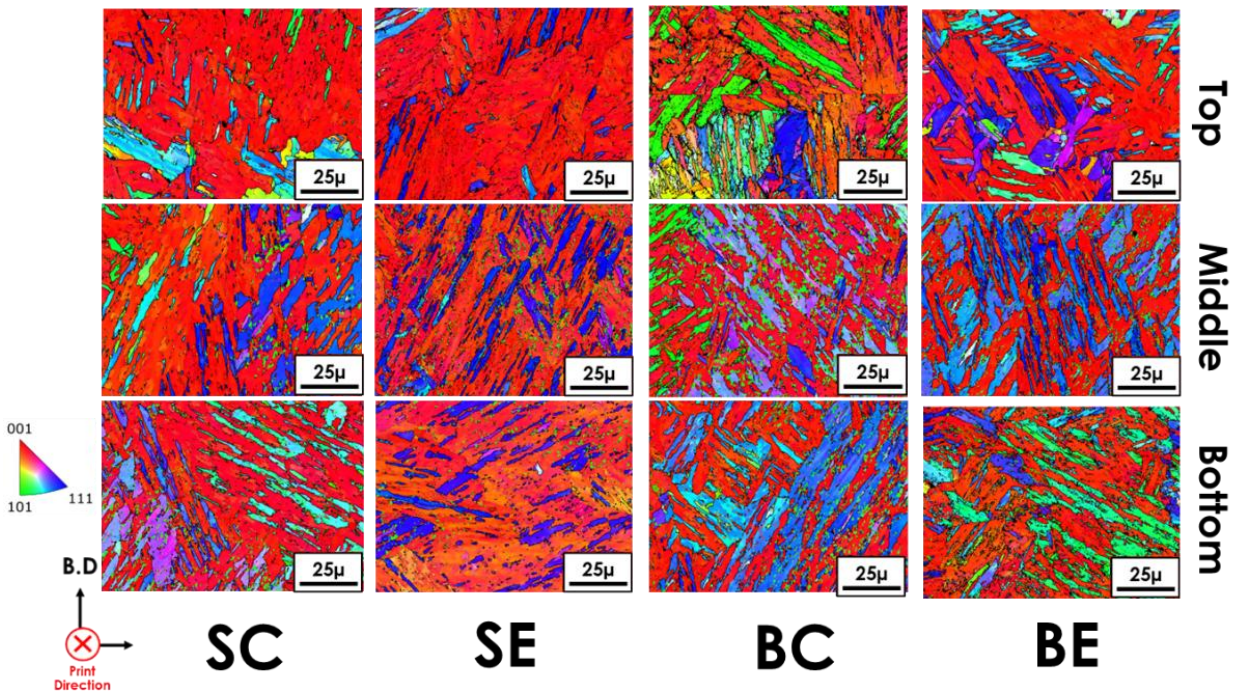

Figure 10: Inverse pole figure map of samples from the top, middle, and bottom regions of the 20-bead thick wall from surface center (SC), surface edge (SE), bulk center (BC), and bulk edge (BE) respectively

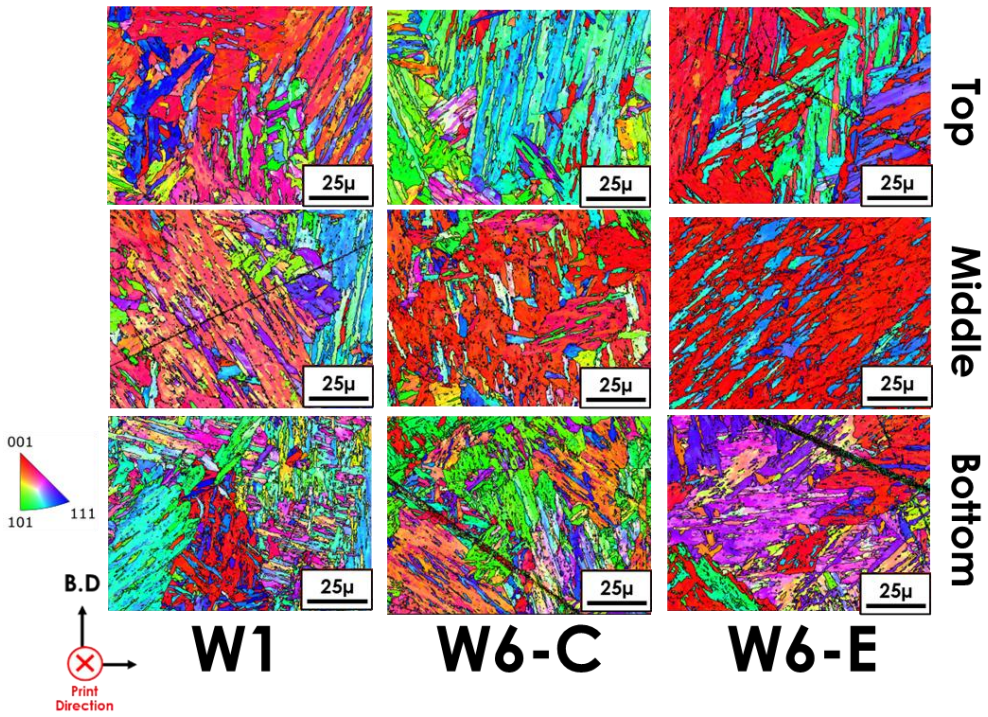

Figure 11: Inverse pole figure map of samples from the top, middle, and bottom regions of the single step (W1), and from the center and edge of 6-stepped (W6-C and W6-E)

Phase transformations in SS 17-4 PH alloy are well known to be greatly influenced by process temperatures and cooling rates [59]. Particularly, the thermal histories characteristic to additive

manufacturing processes are considered having a significant impact on phase fractions in final microstructures, which further impact hardness and mechanical properties of final part [6]. Martensite phase formation is initiated when cooled below the martensitic start temperature (Ms) during continuous cooling, and martensitic transformation fully completes when cooled below martensite finish temperature (M_F) [65, 66]. However, the chemical composition of a given alloy also determines the extent of martensitic transformation. Depending on the carbon composition in a given alloy, it is possible for retained austenite to exist in the microstructure due to suppression of M_F below room temperature [66]. On the other hand, reversed austenite has a tendency to form when aged at temperatures higher than the lower transition temperature (Ac1) for prolonged periods of time. Phase mapping from EBSD data identified FCC austenitic phase in small fractions (as shown in **Table 3**), generally below 1%. However, a higher concentration of austenitic phase was observed in the middle and lower sections of thick 20-bead builds. Austenite (FCC) phase fraction in the thick 20-bead wall reached up to 12.3% at the middle of the bulk center. Further disccussion on retained austenite and reverse austenite formation in martensitic SS 17-4PH alloy is explained in **Section 5.1**.

Table 3. Summary of %FCC phase fraction in the microstructure of samples from top, middle, and bottom regions of different geometric features

%FCC Phase Fraction				
		Top	**Middle**	**Bottom**
Straight Walls	**2B**	0.18	0.14	0.1
	4B	0.13	0.11	0.08
	8B	0.1	0.06	0.17
Inclined Walls	**2B**	1.02	1.27	0.55
	4B	0.15	0.71	2.36
	8B	0.64	0.34	0.81
20-Bead Wall	**SC**	0.39	3	5.19
	SE	0.24	5.1	4.05
	BC	0.49	12.34	8.14
	BE	0.26	7.2	4.21
Wedge	**W1**	0.09	0.15	0.61
	W6-C	0.06	0.52	0.72
	W6-E	0.11	0.73	0.54

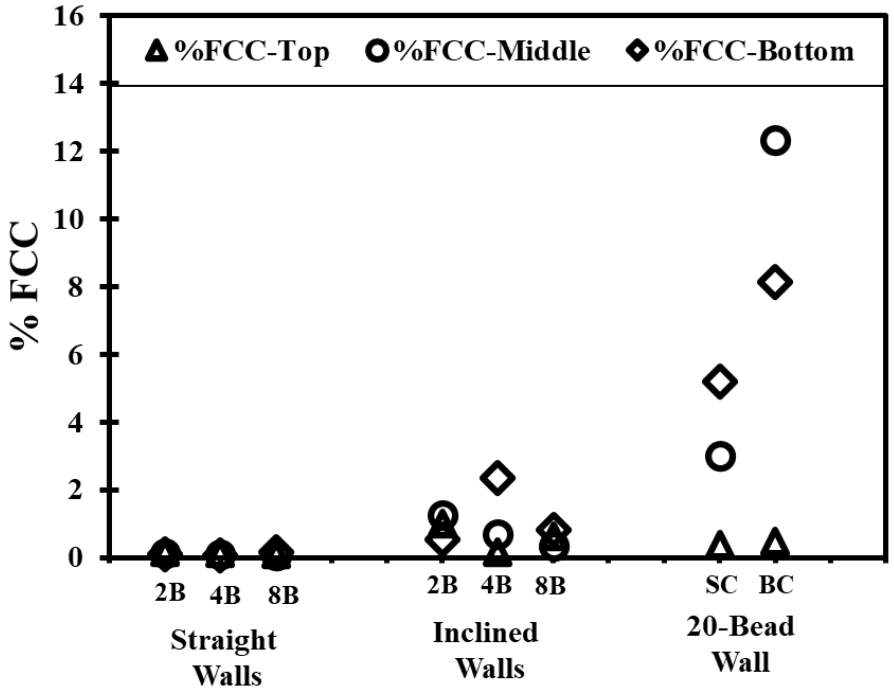

Figure 12: Variation in %FCC phase fraction in the microstructure of samples from top, middle, and bottom regions of different geometric features

Figure 12 summarizes the variation in %FCC (austenite) fraction across the straight walls, inclined walls, and the 20-bead thick wall in top, middle, and bottom section of each wall. Overall, such distinct changes in microstructural phase fractions across different features and geometric locations due to differences in thermal history and cooling rates could reflect in mechanical property variations. This emphasizes the significance of toolpath planning and informed parameter selection for feature-based qualification of WAAM deposited 17-4PH stainless steel components.

4.2 MECHANICAL PROPERTY EVALUATION

Mechanical testing was performed on samples extracted from various WAAM 17-4PH features to assess Vickers microhardness, tensile yield strength, and Charpy V-notch impact toughness. Tests were conducted on straight vertical walls (2B, 4B, 8B), inclined walls (2B, 4B, 8B), and thick vertical walls (20B). Charpy V-notch impact testing and uniaxial tensile testing were performed in accordance with ASTM E8 and ASTM E23 standards respectively.

Vicker's microhardness measurements were performed at the top, middle, and the bottom regions of straight, inclined, and 20-bead thick walls. Across all geometries, average hardness values ranged from a minimum of 326 HV to a maximum of 363 HV (see **Table 4**). Relatively higher values of hardness were generally observed in the mid-sections of thick 20-bead walls. Straight walls and inclined walls showed moderate hardness variation in the range of 326 HV to 343 HV with a slight increase in the middle regions. These variations in hardness across thin and thick walls underscore the direct influence of geometric features and deposition history on the evolving microstructure, reinforcing the need for geometry-specific qualification pathways.

Table 4: Summary of Vickers microhardness in samples from top, middle, and bottom regions of different geometric features

Average Vickers Hardness (HV)				
		Top	**Middle**	**Bottom**
Straight Walls	**2B**	326 ± 10	331 ± 5	327 ± 7
	4B	330 ± 9	338 ± 7	330 ± 6
	8B	338 ± 12	340 ± 9	334 ± 6
Inclined Walls	**2B**	331 ± 11	336 ± 11	330 ± 11
	4B	331 ± 11	343 ± 10	337 ± 9
	8B	339 ± 12	343 ± 11	338 ± 7
20-Bead Wall	**SC**	334 ± 9	363 ± 10	349 ± 12
	SE	334 ± 12	357 ± 11	342 ± 9
	BC	331 ± 10	361 ± 8	344 ± 7
	BE	333 ± 9	355 ± 8	344 ± 6
Wedge	**W1**	330 ± 10	333 ± 7	333 ± 18
	W6-C	334 ± 12	340 ± 15	341 ± 14
	W6-E	328 ± 11	340 ± 10	339 ± 14

The wedge feature did not show noticeable differences in Vickers hardness as compared to the straight walls, despite transitioning from thin to thick walls across the wedge geometry. Hence further analysis of mechanical properties was limited to just the straight walls, inclined walls, and the 20-bead thick wall. **Figure 13** correlates the variation in %FCC fraction with variations in Vickers hardness. It was observed that a rise in %FCC fraction especially in the 20-bead thick walls is concurrent with a rise in hardness values.

An increased austenitic phase fraction in the bottom of the thick 20-bead straight walls was observed. This higher %FCC in the bulk and in the center, compared to the surface and the edge of the 20-bead thick wall can be attributed to higher heat retention in the bulk and center regions. However, this did not translate to a significantly increased Vicker's hardness measurements in these regions. This report emphasizes the effect of intrinsic heat treatment on microstructure and mechanical properties for geometric features printed using the same process parameters. The strengthening mechanism for this material system (SS 17-4PH) is an interplay between hardening from precipitation of copper-rich phases (due to aging) and softening from the formation of reverse austenite (due to chemical segregation). The sensitivity of mechanical properties to these competing mechanisms has not been emphasized in this report and needs to be studied further in detail.

Tensile samples were machined from horizontal, vertical, and 45° orientations. Each had a gauge length of 0.640" and a diameter of 0.160". The extensometer was removed from the samples post-yielding to avoid damage to the equipment during fracture. Tensile testing samples were machined with orientations parallel and perpendicular to the build from the middle regions of the straight walls, inclined walls, and the 20-bead thick wall.

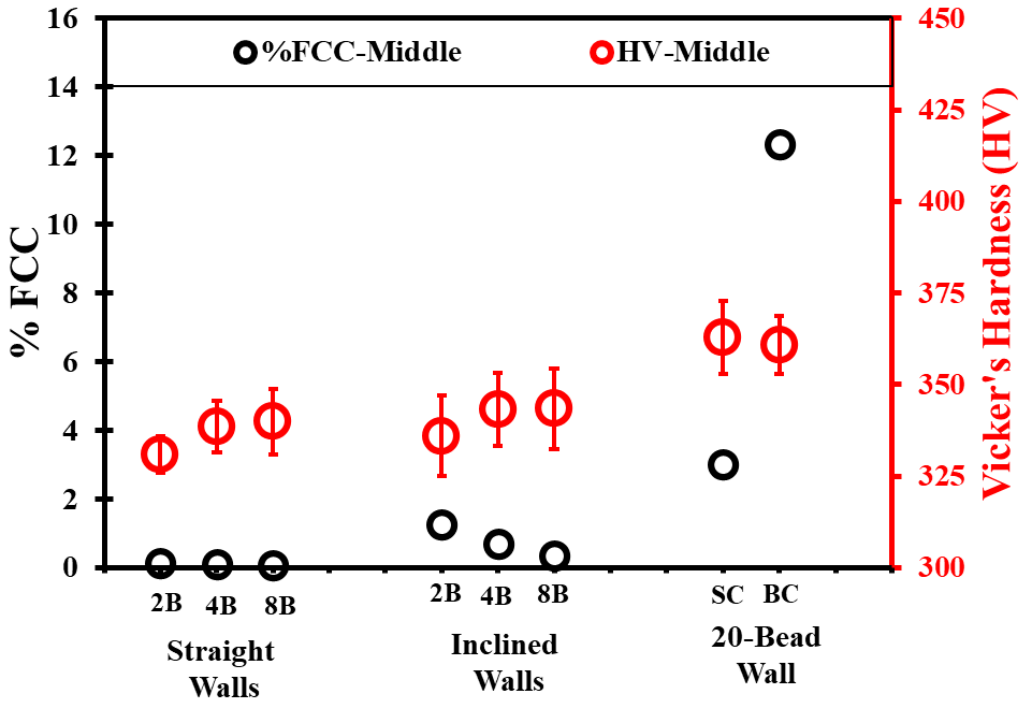

Figure 13: Plot depicting the variation in %FCC fraction and Vickers hardness in samples extracted from the middle of straight walls, inclined walls, and the 20-bead thick wall

0.2% yield strength data ranged from an average minimum of 446 MPa in the 2-bead straight wall to a maximum average of 1003 MPa in the 20-bead thick wall, as shown in **Figure 14**. 20-bead thick walls showed elevated yield strength, likely due to cumulative heat exposure from repeated layer deposition, resulting in stabilized martensitic microstructures clubbed with Cu precipitation from intrinsic heat treatment as proposed by Lyu et. al. [31]. The Vicker's hardness measurements from features deposited in this study ranged from 325-365 HV, whereas the tensile yield strength ranged from 450-1000 MPa. From Table 1, we see that past researchers have observed hardness values in the range of 320-370H V and yield strength in the range of 600-900 MPa. The large spread in the range of yield strength values as well the elevated yield strength observed in the 20-bead thick walls re-emphasize the need the feature-based qualification of large-scale WAAM components – especially for thermally sensitive materials like SS 17-4PH. This anisotropy and spread in yield strength across different geometric features emphasize the heterogeneity in microstructure owing to differences in thermal histories.

These results validate the central hypothesis of the FBQ approach: mechanical properties in WAAM 17-4PH builds are highly location-dependent, influenced by both the geometry of the feature and the resulting thermal history. These findings further underscore the critical role of process planning, including bead deposition sequence and interpass temperature control, in achieving uniform mechanical performance across complex geometries.

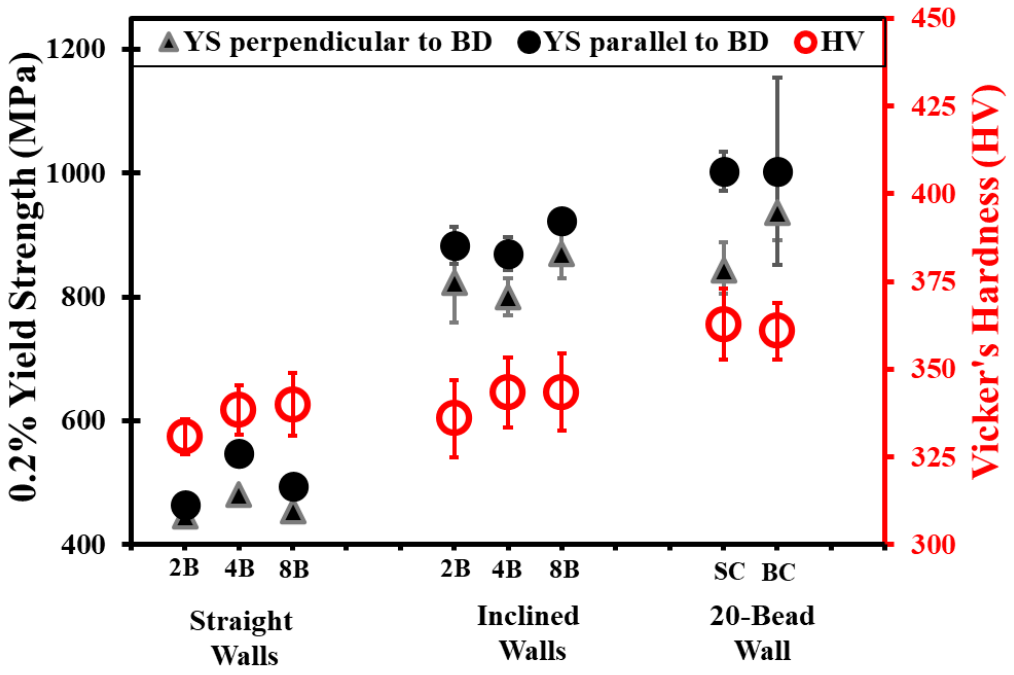

Figure 14: Plot depicting the variation in 0.2% tensile yield strength and Vickers hardness in samples extracted from the middle of straight walls, inclined walls, and the 20-bead thick wall

Additionally, Charpy V-notch impact specimens were extracted from the middle regions of straight walls, inclined walls, and 20-bead thick wall in two different orientations - parallel to the build direction and perpendicular to the build direction. **Table 5** lists the energy absorbed by each sample. In general, there were no distinct trends in the absorbed energies of Charpy V-notch samples, as compared to those seen the Vickers hardness and tensile yield strength data. Samples from the 20-bead thick walls and from the 4-bead inclined walls seemed to fail prematurely. Further fractography is required to identify the cause of failure in these samples. Microstructural heterogeneity, porosity, inclusions, and precipitates are known stress concentrators that can act as sites for crack initiation and propagation [68, 69].

Table 5. Summary of Charpy impact energy absorbed in samples extracted from the middle of straight walls, inclined walls, and the 20-bead thick wall and tested at room temperature

Impact Energy (Ft-Lbs) of samples from the middle region of each feature					
Feature Type		**Perpendicular to BD**		**Parallel to BD**	
		Average	**SD**	**Average**	**SD**
Straight Walls	**2B**	30	1	33	1
	4B	32	2	32	1
	8B	27	3	32	1
Inclined Walls	**2B**	28	2	32	2
	4B	N/A	N/A	28	1
	8B	30	1	36	2

20-Bead Wall	**SC**	15	11	4	0
	BC	17	11	5	1

4.3 IN-SITU MONITORING, SIMULATION, AND THERMAL MODELING

Real-time thermal monitoring was conducted to capture temperature evolution during WAAM deposition across all geometric features. However, thermal monitoring techniques such as IR cameras can only capture surface temperature variations, while thermocouples and pyrometers are limited to specific points. To gain insight into temperature evolution throughout the entire part, physics-based thermal simulations were conducted using ABAQUS 2022 for straight walls (2B, 4B, 8B), thick walls (20B), and wedge features. The predicted thermal profiles can then be used to predict metallurgical and mechanical evolutions, including solid phase transformations, distortion, and residual stresses.

In the simulations, the bottom of the baseplate was maintained at 25 °C, while the outer surface of the deposit was subjected to heat convection with a temperature-dependent convective coefficient [69]. The energy input during deposition was modeled using a Goldak volumetric heat source. The tool path and heat source power were directly extracted from the printer's log data, allowing the simulation to accurately capture real printing conditions, including pauses and variations in torch speed and power.

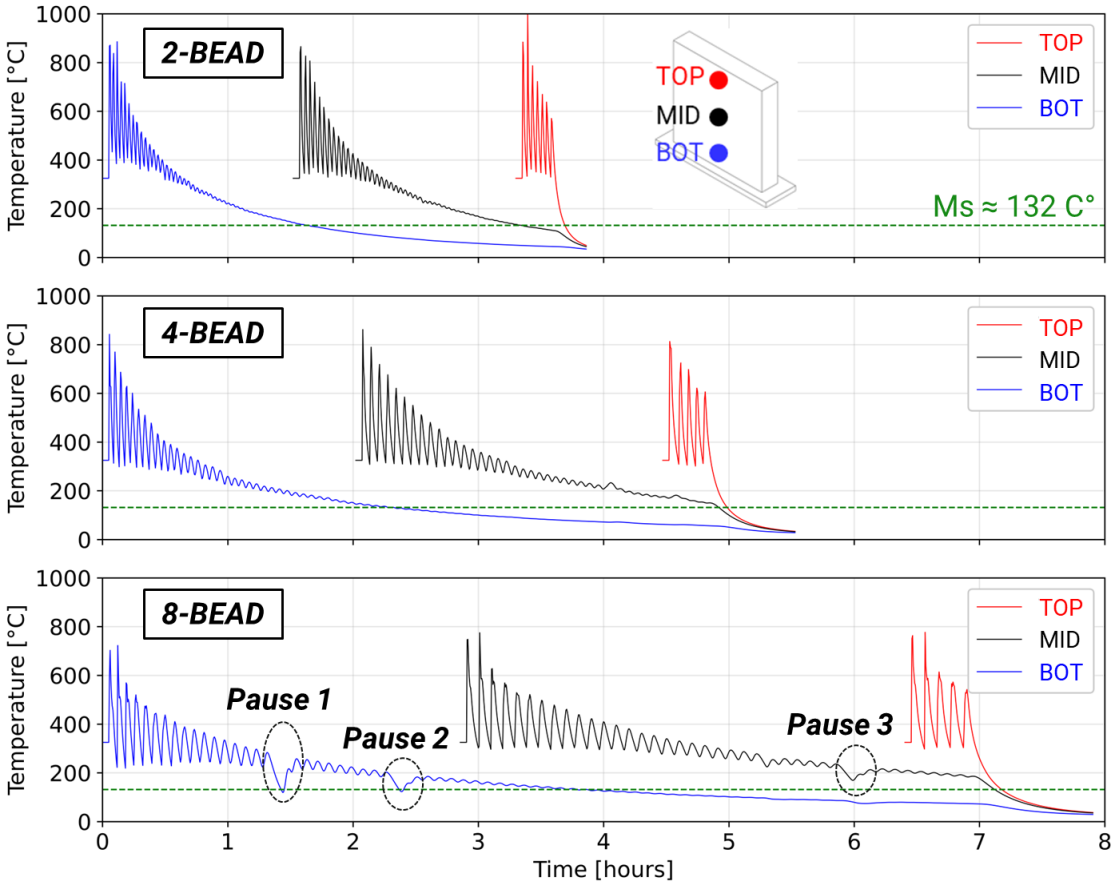

Figure 15: Temperature histories at the top (TOP), middle (MID), and bottom (BOT) locations along the centerline of straight walls with 2-bead (2B), 4-bead (4B), and 8-bead (8B) thicknesses. Three pauses, each lasting approximately 5 minutes, occurred during the deposition of the 8B wall.

The temperature histories at three locations along the centerline of the straight walls (2B, 4B, 8B)—specifically in the top (TOP), middle (MID), and bottom (BOT) regions—were extracted, as shown in **Figure 15**. The 2B and 4B walls were printed continuously, while the 8B wall experienced several pauses, each lasting approximately 5 minutes. Such pauses during WAAM can occur due to maintenance, abnormality checks, or part replacement, and they can significantly alter the thermal history of the deposit. Therefore, incorporating these pauses into the simulations is essential for accurate temperature predictions. Overall, due to cumulative heat buildup, the cooling rate is highest at the top region, moderate in the middle, and lowest at the bottom. As a result, the bottom regions experienced extended periods above the martensite start temperature (Ms), which is assumed to be approximately 132 °C for 17-4PH.

Similarly, the temperature histories at three locations (top, middle, and bottom) along the centerline of the 20B wall are shown in **Figure 16**. As with the 2B, 4B, and 8B walls, the cooling rate in the 20B wall decreases from top to bottom. The 20B wall was fabricated over three days, with deposition times of approximately 5.6 hours, 5.1 hours, and 2.7 hours on each respective day. Between print sessions, the printer was turned off, and as a result, the part cooled to ambient temperature before printing resumed the next day. When the deposition restarted, the previously deposited material was reheated from ambient temperature. Notably, the bottom (BOT) location, which was deposited on the first day, remained above Ms for about 3.4 hours during the second day's printing. Similarly, the middle (MID) location, deposited on the second day, stayed above Ms for approximately 2.7 hours during the third day's printing. In-situ aging and partial austenite reversion usually occurs at temperatures closer to ~500°C, potentially impacting the microstructure and mechanical properties of the deposit.

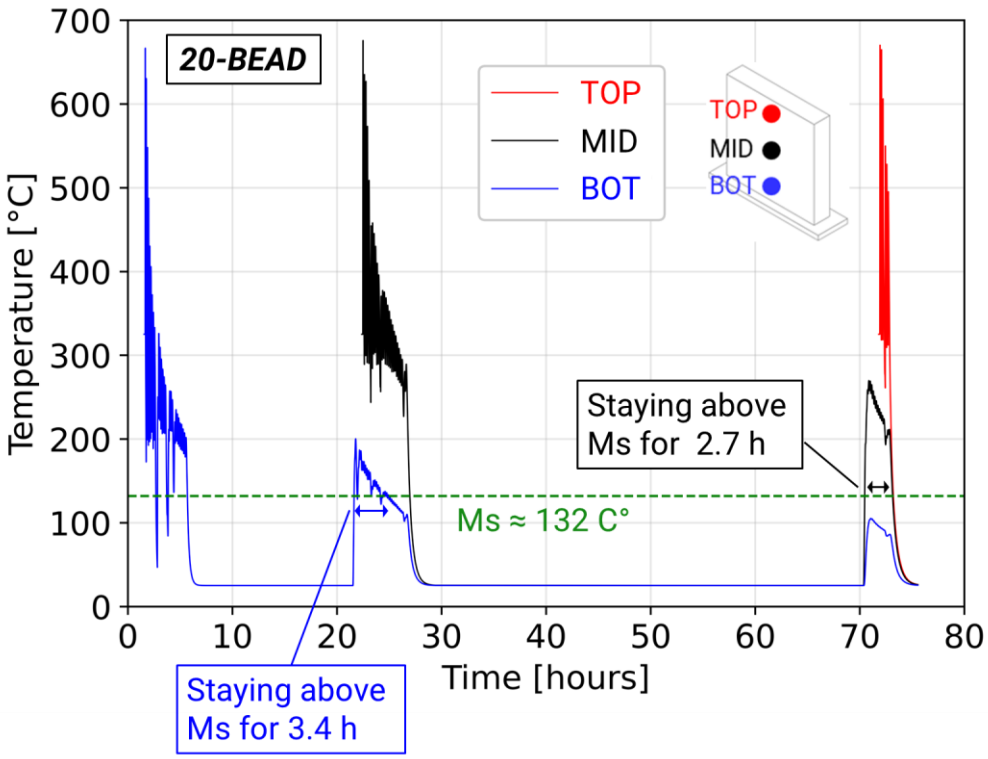

Figure 16: Temperature histories at the top (TOP), middle (MID), and bottom (BOT) locations along the centerline of the wall with 20-bead (20B) thicknesses.

4.4 DATA VISUALIZATION VIA INTEGRATION WITH PELICAN GUI PLATFORM

Pelican is data-driven analysis tool for designed for advanced manufacturing processes, providing a platform for: recording and viewing machine and operational meta- and log-data; exploring and visualizing multimodal, spatiotemporal process monitoring data streams; spatially and temporally registering ex situ characterization results with in situ sensing data for comparative analyses; training machine learning models to detect process anomalies and predict part quality; benchmarking trained models to quantify performance.

Pelican, an alpha version of which is expected to be available in FY26, is a flexible analysis tool designed for spatiotemporal datasets of arbitrary origin, structure, and resolution. Available with both a graphical user interface (GUI) and a companion application programming interface (API), Pelican is built first for Directed Energy Deposition (DED) processes, where a host of multimodal sensor data (melt pool cameras, acoustic emissions, etc.) can be linked to spatial quality (e.g., X-ray computed tomography, dimensional conformance scans, microstructural data). In addition to its suite of spatiotemporal visualizations, Pelican provides a flexible architecture for developing and deploying advanced analytical tools (e.g., computer vision algorithms, machine learning models) aimed at assessing process and part quality using the multi-modal data sets. **Figure 17** provides a summary of the Pelican Operation Window, highlighting updates to the various metadata tracking and data visualization widgets available from the GUI.

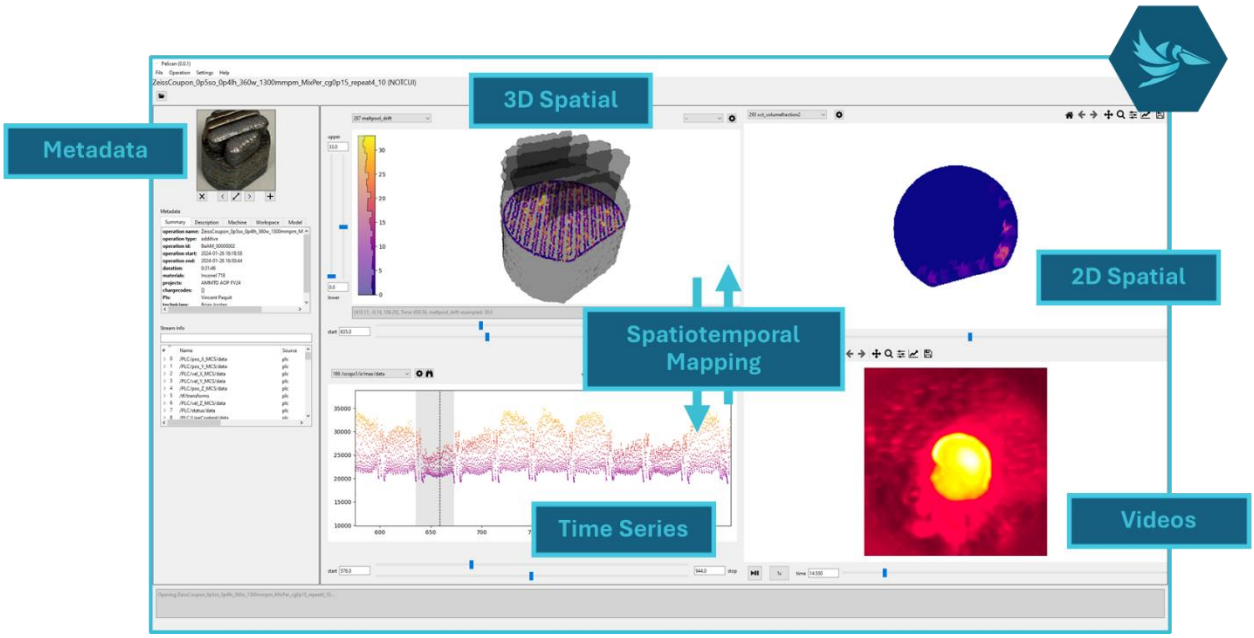

Figure 17: Summary of the Pelican Operation Window, highlighting the various metadata tracking and data visualization widgets.

Pelican is designed to be a general analysis tool agnostic to sensor-, material-, and DED-platform being evaluated. For example, the data shown in **Figure 18** corresponds to data collected during a laser-based, blown-powder DED process, but Pelican can just as easily be applied to WAAM DED processes.

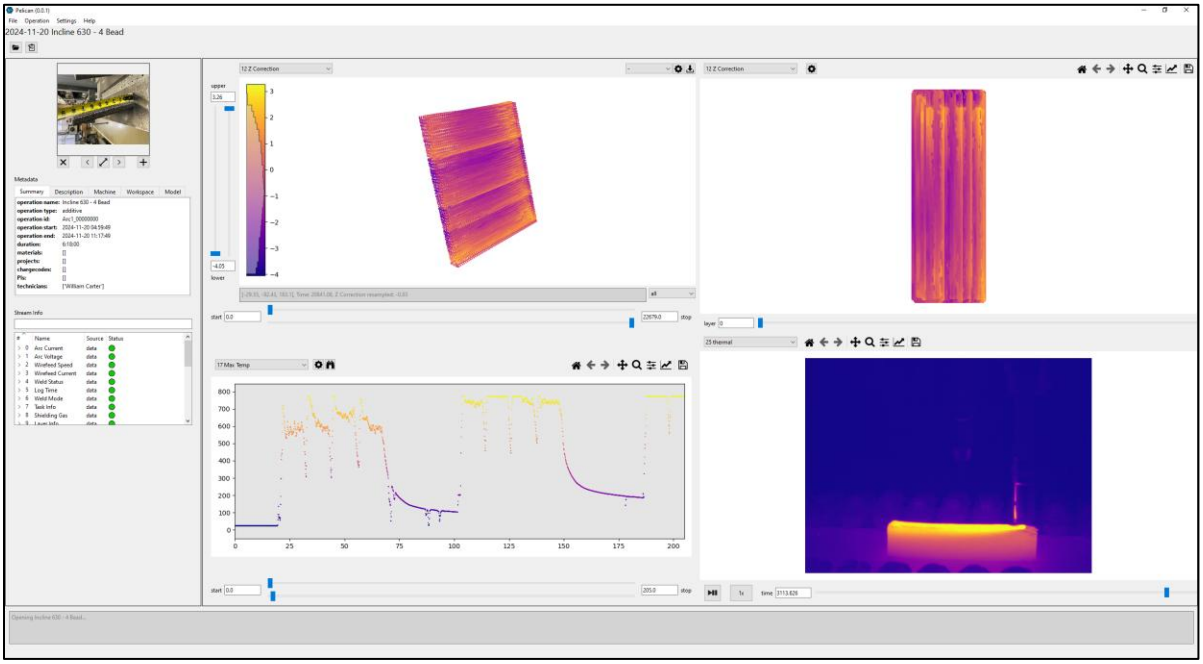

Figure 18: Pelican operation window showing select data visualization for WAAM process monitoring data collected at the MDF.

Figure 18 shows a series of interactive visualization tool for data collected on the MDF's Arc1 printer, from which positional information, arc voltage and current, wire feed rates and currents, and various other time series data can be ingested and visualized. Off-axis video data, such as the thermal imaging data shown in **Figure 18**, can also be ingested and visualized within the context of the build. Such visualizations are designed to facilitate context-driven data exploration to readily identify process anomalies in multi-modal data and identify regions of interest for post-build metallurgical investigation.

5. DISCUSSION

5.1 AUSTENITIC TRANSFORMATIONS IN WAAM OF SS 17-4PH

WAAM as a process is characteristic of unique thermal phenomena such as cyclic heating and cooling, and thermal buildup which can lead to strong thermal gradients across a given component. Such phenomena during processing can cause microstructural variations in thermally sensitive material systems like SS17-4PH that toughen by martensitic transformation and segregation of Cu-rich precipitates. In SS 17-4PH, austenite can show up in two different ways during and after processing [70, 71]:

1. **Retained austenite** is formed by incomplete martensitic transformation due to a suppression in M_f temperature below the room temperature, leading to retained austenite in the microstructure after solidification

2. **Reversed austenite** on the other hand is a phase that forms during tempering or thermal cycling, where martensite changes back to austenite under certain thermodynamic conditions.

Both these forms of austenite can have a big impact on how WAAM 17-4PH parts perform and how stable their microstructure is.

Retained austenite forms because of incomplete martensitic transformation during cooling due to the non-equilibrated enrichment of alloying metals like Ni, Cu, Mn, and C which lower martensite finish temperature (M_F) thereby stabilizing the face-centered cubic (FCC) structure at room temperature [70-72]. Retained austenite tends to segregate in interdendritic zones that are stabilized by elements like Ni and Cu. This phase is often metastable and has the potential to transform into martensite when plastically deformed. Such a phenomena of martensitic transformation under plastic deformation is called transformation-induced plasticity (TRIP) [33, 73-75]. Retained austenite has a big effect on the characteristics of materials, such as making them more ductile and tough through the transformation-induced plasticity (TRIP) effect. However, higher concentrations and inhomogeneous distribution can lower the yield strength.

Transformed martensite has the potential to revert to austenite after being exposed to temperatures above the lower transformation temperature (Ac1) for a long duration. Diffusion mechanisms control this transition, which usually occurs between 400°C and 600°C, depending on the local composition [76]. Reverse austenite formation is accelerated by thermal cycling and intrinsic heat treatment (IHT) due to poor thermal conductivity pathways. Reverse austenite usually has finer, more evenly shaped grains with fewer dislocation [70-72]. The results from 20 bead thick wall

structures in this project show evidence for the formation of reverse austenite. The FCC content in the middle and lower parts of these structures went up to 12.3%, as shown in **Table 3,** while the KAM values went down. This suggests a decrease in dislocation density and formation of reverse austenite. These observations are in line with phenomena observed in past literature, were similar changes in phase distribution of 17-4PH stainless steel was seen to be impacted by intrinsic heat treatment during WAAM or multi-pass welding of SS 17-4PH alloy [32, 77].

5.2 PROCESSING-STRUCTURE-PROPERTY (PSP) CORRELATION

Experimental findings and simulation results in conjunction with in-situ data monitoring enable the possibility to map processing-structure-property (PSP) relationships in SS 17-4PH processed via WAAM. This section dives deeper into the effect of inherent process conditions and geometric features on microstructure and mechanical behavior of as-printed WAAM SS 17-4PH.

In WAAM, each layer that is deposited causes the one below it to heat up to an elevated temperature. This creates unique thermal cycles that are different for each location in each build as shown in **Figure 19**. The bottom part of a build that is closer to the substrate cools down faster since the base plate acts as heat sink allowing for heat transfer via conduction. However, further deposition of layers on the bottom section of the components results in thermal cycling. The middle section of the components cools down primarily by convection heat loss to the ambient atmosphere, thereby making the cooling rates in the middle compared to the layers closer to the substrate. This middle section also experiences cycling heating and cooling from the layers deposited on top. This thermal cycling along with slower cooling rates lead to the accumulation of thermal mass in the middle section of a WAAM build, which becomes more prominent with increasing thickness of the build. The top of a WAAM component cools down much faster due to convection and radiation heat transfer, while also being devoid of any further thermal cycling.

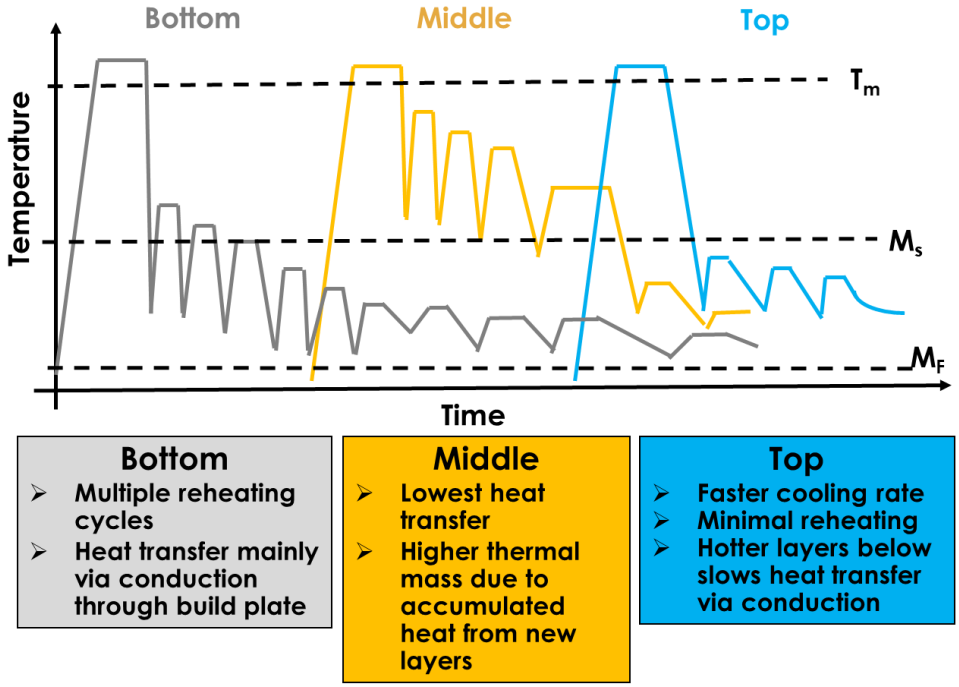

Figure 19: Schematic depicting the variations in location-specific cooling rates and thermal cycles experienced during WAAM deposition

These thermally different zones make it possible for both retained and reverse austenite to exist in the same component. Past researchers have observed similar phenomenon in WAAM [78] and LP-DED [79] . In-situ temperature data from the results showed the middle section of the 20 bead wall staying above Ms for a long duration. This processing artifact corroborates the formation of reverse austenite as evident in EBSD phase analysis data. Moreover, the middle section of the 20-bead wall also exhibited higher hardness, due to in-situ aging and precipitation during reversed austenitic transformation. Additionally, the Pelican platform makes real-time contextual visualization possible, which aids in tracing the path from processing events to microstructural variations to mechanical consequences.

To summarize, the final microstructure and mechanical properties of WAAM SS 17-4PH show a clear dependency on processing conditions. Reheating and thermal accumulation causes elemental segregation thereby initiating in-situ aging, precipitation, and reversed austenitic transformation. More importantly, geometric features were seen to play a significant role in determining thermal histories and solidification kinetics leading to variations in phase compositions and consequent property anisotropy. Section 5.3 elaborates on the implications of the findings from this project for feature-based qualification of individual simple geometries.

5.3 IMPLICATIONS FOR FEATURE-BASED QUALIFICATION

More often than not, traditional qualification procedures rely on bulk coupon testing or full component certification. These might not be the best choice of qualification methods for WAAM, especially considering the wide range of variations in thermal histories across large-scale metal components. The use of simplified geometric characteristics (like those used in this study) makes it easier to systematically look at localized effects. Such a feature-based qualification method focuses on deconvoluting complex components into simple geometric-features to understand process-dependent thermal histories and their effects, thereby significantly reducing the time, cost, and scope of qualification.

This study aims to analyze different features of simple geometries that were meant to represent the thermal conditions that real-world application-based components would experience. Straight walls showed areas that were vertical with a constant thickness whereas inclined walls are representative of sloped or cantilevered sections. 20 bead wall was used to model thicker sections of a component which could potentially represent the bulk properties of parts fabricated via WAAM, whereas the wedge geometry delineated the thermal transition between thicker and thinner parts. These features - straight, inclined, thick, and wedge walls emphasize on the most common setbacks WAAM components suffer from, in real life. Challenges such as heat build-up at thick cross-sections, and location-specific cooling rates are identified, while elaborating on its impact on mechanical property variations.

By finding the local microstructure-property connections, these traits make it possible to make localized PSP predictions without having to test the whole component. Using EBSD and mechanical property data from strategic locations, we can describe PSP relationships for a component in 3D space, making it easier for digital qualification. Data visualization of thermal

and process-specific events in the spatiotemporal realm using Pelican GUI will create a strong framework for a real-time, context-oriented qualification process. Ultimately, developing a digital model of traits that can predict PSP relationships based on process parameter and individual geometric features in a complex component will not only accelerate process qualification, but also help improve part quality by taking into consideration the thermal histories during path planning and deposition.

6. CONCLUSIONS AND FUTURE WORK

In summary, wire arc additive manufacturing (WAAM) of SS 17-4PH alloy exhibits variations in microstructural phase evolution and mechanical properties across different locations in a large-scale component. These variations arise from thermal profiles, cooling rates, and heat accumulation kinetics in different geometric features. In-situ thermal monitoring, microstructural characterization, mechanical property evaluation, along with thermal simulations and data visualization, made it possible to analyze processing-structure-property (PSP) relationships across a range of build geometries. Cumulative thermal effects in the middle portion of the thicker 20-bead wall showed higher hardness which was attributed to in-situ ageing and reversed austenite transformation from continuous thermal cycling and heat accumulation.

Combining in-situ thermal data with post-build EBSD and hardness measurements show that modeling techniques may be used to accurately predict and validate the behavior of retained austenite in spatiotemporal space. Adding data visualization using Pelican GUI could make it easier to see and understand different data streams, which has the potential to lay the groundwork for a digital qualification framework. The results of this study prove that feature-based qualification in WAAM is both possible and necessary to accelerate fabrication of reliable large-scale SS 17-4PH components. The information collected on thermal variations, microstructural development, and mechanical anisotropy as a function of geometric feature and location lays the groundwork for future work, which will shift the focus from single features to composite components and digital validation methods.

Future work should build on these foundations by moving from single-feature qualification to multi-feature part-level validation while understanding how differences in as-printed parts translate to solutionized and aged components. Part qualification (PQ) is a critical process involving evaluation of a part's suitability for fabrication via WAAM while ensuring it meets performance requirements. PQ considers factors such part complexity, size, material, machining requirements etc. Such qualification methodologies will lay the foundation for robust post-process measurements and testing critical components for defense, aerospace, and medical applications

Additionally, future work should focus on a larger range of alloy systems such as Inconel 625, Ti-6Al-4V, and PH13-8Mo. Finally, developing and scaling-up Pelican GUI for real-time prediction analytics could help predict defects and microstructural variations across complex components. These next steps will enable automated, real-time qualifying methods based on the ideas of materials science, thermal physics, and data analytics for WAAM be integrated into structural and critical applications in the defense and manufacturing industries.

REFERENCES

1. Pereira, A., et al., *Experimental Study on the Manufacturing of Steel Inclined Walls by Directed Energy Deposition Based on Dimensional and 3D Surface Roughness Measurements.* Materials, 2022. **15**(14).
2. Prajadhiana, K.P., et al., *Distortion Analysis Method for Wire Arc Additive Manufacturing Component Using Thermomechanical Computation with Enhanced Separation and Deposition Algorithm.* 3d Printing and Additive Manufacturing, 2024. **11**(4): p. e1616-e1628.
3. Xia, J., et al., *Bifurcation of a topological skyrmion string.* Physical Review B, 2022. **105**(21).
4. Thompson, S.M., et al., *An overview of Direct Laser Deposition for additive manufacturing; Part I: Transport phenomena, modeling and diagnostics.* Additive Manufacturing, 2015. **8**: p. 36-62.
5. Shamsaei, N., et al., *An overview overview of Direct Laser Deposition for additive manufacturing; Part II: Mechanical behavior, process parameter optimization and control.* Additive Manufacturing, 2015. **8**: p. 12-35.
6. Caballero, A., et al., *Wire plus Arc Additive Manufacture of 17-4 PH stainless steel: Effect of different processing conditions on microstructure, hardness, and tensile strength.* Journal of Materials Processing Technology, 2019. **268**: p. 54-62.
7. Jin, W.W., et al., *Wire Arc Additive Manufacturing of Stainless Steels: A Review.* Applied Sciences-Basel, 2020. **10**(5).
8. Ding, D.H., et al., *A multi-bead overlapping model for robotic wire and arc additive manufacturing (WAAM).* Robotics and Computer-Integrated Manufacturing, 2015. **31**: p. 101-110.
9. Chen, B. and J. Mazumder, *Role of process parameters during additive manufacturing by direct metal deposition of Inconel 718.* Rapid Prototyping Journal, 2017. **23**(5): p. 919-929.
10. Yusuf, S.M., S. Cutler, and N. Gao, *Review: The Impact of Metal Additive Manufacturing on the Aerospace Industry.* Metals, 2019. **9**(12).
11. Seede, R., et al., *An ultra-high strength martensitic steel fabricated using selective laser melting additive manufacturing: Densification, microstructure, and mechanical properties.* Acta Materialia, 2020. **186**: p. 199-214.
12. Available from: https://ampower.eu/infographics/metal-additive-manufacturing/.
13. Rodrigues, T.A., et al., *Current Status and Perspectives on Wire and Arc Additive Manufacturing (WAAM).* Materials, 2019. **12**(7).
14. Thapliyal, S., *Challenges associated with the wire arc additive manufacturing (WAAM) of aluminum alloys.* Materials Research Express, 2019. **6**(11).
15. Albannai, A.I., *A brief review on the common defects in wire arc additive manufacturing.* Int. J. Curr. Sci. Res. Rev, 2022. **5**: p. 4556-4576.
16. Ghaffari, M., A. Vahedi Nemani, and A. Nasiri, *Microstructure and mechanical behavior of PH 13–8Mo martensitic stainless steel fabricated by wire arc additive manufacturing.* Additive Manufacturing, 2022. **49**: p. 102374.
17. Martina, F., et al., *Tandem metal inert gas process for high productivity wire arc additive manufacturing in stainless steel.* Additive Manufacturing, 2019. **25**: p. 545-550.
18. Queguineur, A., et al., *Wire arc additive manufacturing of thin and thick walls made of duplex stainless steel.* International Journal of Advanced Manufacturing Technology, 2023. **127**(1-2): p. 381-400.
19. Frazier, W.E., *Metal Additive Manufacturing: A Review.* Journal of Materials Engineering and Performance, 2014. **23**(6): p. 1917-1928.
20. McAndrew, A.R., et al., *Interpass rolling of Ti-6Al-4V wire + arc additively manufactured features for microstructural refinement.* Additive Manufacturing, 2018. **21**: p. 340-349.
21. Williams, S.W., et al., *Wire plus Arc Additive Manufacturing.* Materials Science and Technology, 2016. **32**(7): p. 641-647.

22. Wu, B.T., et al., *The anisotropic corrosion behaviour of wire arc additive manufactured Ti-6A1-4V alloy in 3.5% NaCl solution.* Corrosion Science, 2018. **137**: p. 176-183.
23. Gu, J.L., et al., *The strengthening effect of inter-layer cold working and post-deposition heat treatment on the additively manufactured Al-6.3Cu alloy.* Materials Science and Engineering a-Structural Materials Properties Microstructure and Processing, 2016. **651**: p. 18-26.
24. Zou, X.D., et al., *Wire plus Arc Additive Manufacturing and Heat Treatment of Super Martensitic Stainless Steel with a Refined Microstructure and Excellent Mechanical Properties.* Materials, 2022. **15**(7).
25. Xu, F.J., et al., *Microstructural Evolution and Mechanical Properties of Inconel 625 Alloy during Pulsed Plasma Arc Deposition Process.* Journal of Materials Science & Technology, 2013. **29**(5): p. 480-488.
26. Bhaduri, A.K., et al., *Optimized postweld heat treatment procedures for 17-4 PH stainless steels.* Welding Journal, 1995. **74**: p. Medium: X; Size: pp. 153.s-159.s 2009-12-16.
27. Vagi, J.J., R.M. Evans, and D.C. Martin, *Welding of Precipitation-Hardening Stainless Steels*. 1968: United States.
28. DebRoy, T., et al., *Additive manufacturing of metallic components - Process, structure and properties.* Progress in Materials Science, 2018. **92**: p. 112-224.
29. Nezhadfar, P.D., et al., *Microstructure and Deformation Behavior of Additively Manufactured 17-4 Stainless Steel: Laser Powder Bed Fusion vs. Laser Powder Directed Energy Deposition.* Jom, 2022. **74**(3): p. 1136-1148.
30. Zhou, T., et al., *Microstructure control during deposition and post-treatment to optimize mechanical properties of wire-arc additively manufactured 17-4 PH stainless steel.* Additive Manufacturing, 2022. **58**.
31. Lyu, Z.W., et al., *Simultaneous enhancements of strength and ductility of wire arc additive manufactured 17-4PH steel via intrinsic heat treatment.* Journal of Materials Processing Technology, 2023. **321**.
32. Mohammadi, J., et al., *Microstructure and mechanical properties of 17-4 PH stainless steel fabricated by gas metal wire arc additive manufacturing.* Materials Today Communications, 2024. **39**.
33. Sabooni, S., et al., *Laser powder bed fusion of 17-4 PH stainless steel: A comparative study on the effect of heat treatment on the microstructure evolution and mechanical properties.* Additive Manufacturing, 2021. **46**.
34. Moyle, M.S., et al., *Evidence of Cu clustering as a function of laser power during laser powder bed fusion of 17-4 PH stainless steel.* Scripta Materialia, 2022. **219**.
35. Nezhadfar, P.D., et al., *Fatigue behavior of additively manufactured 17-4 PH stainless steel: Synergistic effects of surface roughness and heat treatment.* International Journal of Fatigue, 2019. **124**: p. 188-204.
36. Sabzi, H.E., et al., *Genetic design of precipitation-hardening stainless steels for additive manufacturing.* Acta Materialia, 2024. **274**: p. 120018.
37. Mathoho, I., et al., *Impact of DED process parameters on the metallurgical characteristics of 17-4 PH SS deposited using DED.* Cirp Journal of Manufacturing Science and Technology, 2020. **31**: p. 450-458.
38. Muslim, T., et al., *Laser metal deposition of 17-4 PH stainless steel: Geometrical, microstructural, and mechanical properties investigation for structural applications.* Cirp Journal of Manufacturing Science and Technology, 2023. **41**: p. 69-79.
39. Herzog, D., et al., *Additive manufacturing of metals.* Acta Materialia, 2016. **117**: p. 371-392.
40. Lippold, J.C., *Recent developments in the understanding of stainless steel welding metallurgy.* Trends in Welding Research, Proceedings, 2003: p. 1-10.
41. Baufeld, B., O. van der Biest, and R. Gault, *Microstructure of Ti-6Al-4V specimens produced by shaped metal deposition.* International Journal of Materials Research, 2009. **100**(11): p. 1536-1542.

42. Lee, Y., et al., *Effect of Interlayer Cooling Time, Constraint and Tool Path Strategy on Deformation of Large Components Made by Laser Metal Deposition with Wire.* Applied Sciences-Basel, 2019. **9**(23).
43. Kumar, P. and K. Maji, *Experimental investigations and parametric effects on depositions of super duplex stainless steel in wire arc additive manufacturing.* Proceedings of the Institution of Mechanical Engineers Part E-Journal of Process Mechanical Engineering, 2023.
44. Zhang, Y.Q., F.J. Cheng, and S.J. Wu, *The microstructure and mechanical properties of duplex stainless steel components fabricated via flux-cored wire arc-additive manufacturing.* Journal of Manufacturing Processes, 2021. **69**: p. 204-214.
45. Hejripour, F., et al., *Thermal modeling and characterization of wire arc additive manufactured duplex stainless steel.* Journal of Materials Processing Technology, 2019. **272**: p. 58-71.
46. Sültzer, J., et al., *GMAW Cold Wire Technology for Adjusting the Ferrite-Austenite Ratio of Wire and Arc Additive Manufactured Duplex Stainless Steel Components.* Metals, 2019. **9**(5).
47. Zhou, J.G., D. Herscovici, and C.C. Chen, *Parametric process optimization to improve the accuracy of rapid prototyped stereolithography parts.* International Journal of Machine Tools & Manufacture, 2000. **40**(3): p. 363-379.
48. Campanelli, S.L., et al., *Statistical analysis of the stereolithographic process to improve the accuracy.* Computer-Aided Design, 2007. **39**(1): p. 80-86.
49. Mahesh, M., et al., *A six-sigma approach for benchmarking of RP&M processes.* International Journal of Advanced Manufacturing Technology, 2006. **31**(3-4): p. 374-387.
50. Lanzotti, A., et al., *On the Geometric Accuracy of RepRap Open-Source Three-Dimensional Printer.* Journal of Mechanical Design, 2015. **137**(10).
51. Cruz Sanchez, F.A., et al., *Towards a standard experimental protocol for open source additive manufacturing.* Virtual and Physical Prototyping, 2014. **9**(3): p. 151-167.
52. Pennington, R.C., N.L. Hoekstra, and J.L. Newcomer, *Significant factors in the dimensional accuracy of fused deposition modelling.* Proceedings of the Institution of Mechanical Engineers Part E-Journal of Process Mechanical Engineering, 2005. **219**(E1): p. 89-92.
53. Abu Bakar, N.S., M.R. Alkahari, and H. Boejang, *Analysis on fused deposition modelling performance.* Journal of Zhejiang University-Science A, 2010. **11**(12): p. 972-977.
54. Meisel, N. and C. Williams, *An Investigation of Key Design for Additive Manufacturing Constraints in Multimaterial Three-Dimensional Printing.* Journal of Mechanical Design, 2015. **137**(11).
55. Rebaioli, L. and I. Fassi, *A review on benchmark artifacts for evaluating the geometrical performance of additive manufacturing processes.* International Journal of Advanced Manufacturing Technology, 2017. **93**(5-8): p. 2571-2598.
56. Qin, J., et al., *Research and application of machine learning for additive manufacturing.* Additive Manufacturing, 2022. **52**.
57. Mutahar Safdar , G.L., Padma Polash Paul , Gentry Wood , Yaoyao Fiona Zhao, *Engineering of Additive Manufacturing Features for Data-Driven Solutions*. 2023: Springer Nature Switzerland.
58. Nag, S., et al., *Probabilistic Machine Learning Assisted Feature-Based Qualification of DED Ti64.* Jom, 2021. **73**(10): p. 3064-3081.
59. Ajjarapu, P., et al., *Feature Based Qualification (FBQ) of Wire Arc Additively Manufactured (WAAM) 17-4PH Martensitic Stainless Steels*. 2024, Oak Ridge National Laboratory (ORNL), Oak Ridge, TN (United States): United States. p. Medium: ED; Size: 45 p.
60. Wu, B.T., et al., *A review of the wire arc additive manufacturing of metals: properties, defects and quality improvement.* Journal of Manufacturing Processes, 2018. **35**: p. 127-139.
61. Biserova-Tahchieva, A., et al., *Additive Manufacturing Processes in Selected Corrosion Resistant Materials: A State of Knowledge Review.* Materials, 2023. **16**(5).
62. Shimizu, K. and Z. Nishiyama, *Electron-Microscopic Studies of Martensitic Transformations in Iron-Alloys and Steels.* Metallurgical Transactions, 1972. **3**(5): p. 1055-+.
63. Hsiao, C.N., C.S. Chiou, and J.R. Yang, *Aging reactions in a 17-4 PH stainless steel.* Materials Chemistry and Physics, 2002. **74**(2): p. 134-142.

64. Viswanathan, U.K., S. Banerjee, and R. Krishnan, *Effects of Aging on the Microstructure of 17-4 Ph Stainless-Steel.* Materials Science and Engineering a-Structural Materials Properties Microstructure and Processing, 1988. **104**: p. 181-189.
65. Abrahams, R.A., *The development of high strength corrosion resistant precipitation hardening cast steels*. 2010.
66. Jacob, G., *Prediction of Solidification Phases in Cr-Ni Stainless Steel Alloys Manufactured by Laser Based Powder Bed Fusion Process*. 2018, Advanced Manufacturing Series (NIST AMS), National Institute of Standards and Technology, Gaithersburg, MD.
67. Chi, G., et al., *Crack propagation during Charpy impact toughness testing of Ti−Al−V−Mo−Zr alloy tubes containing equiaxed and lamellar microstructures.* Journal of Alloys and Compounds, 2021. **852**: p. 156581.
68. Isogawa, S., et al., *Improvement of the forgability of 17-4 precipitation hardening stainless steel by ausforming.* Journal of Materials Processing Technology, 1998. **74**(1): p. 298-306.
69. Nycz, A., et al., *Effective residual stress prediction validated with neutron diffraction method for metal large-scale additive manufacturing.* Materials & Design, 2021. **205**.
70. Spigarelli, S., et al., *Short-term creep approach to redefining the role of 17-4PH stainless steel for high-temperature applications.* Scientific Reports, 2024. **14**(1).
71. Wu, L.L., et al., *Effect of Reversed Austenite on the Stress Corrosion Cracking of Modified 17-4PH Stainless Steel.* Corrosion, 2017. **73**(6): p. 704-712.
72. Chen, C.Y., I. Chiang, and Y.C. Kang, *The effect of retained austenite on austenite reversion behavior and corresponding mechanical properties of Ti-Mo precipitation hardening stainless steels.* Journal of Materials Research and Technology-Jmr&T, 2025. **35**: p. 1476-1493.
73. Huang, R.R., et al., *Additive manufacturing of 17-4PH stainless steel: Effect of heat treatment on microstructure evolution and strengthening behavior.* Materials Science and Engineering a-Structural Materials Properties Microstructure and Processing, 2024. **908**.
74. Jones, J., A. Vafadar, and R. Hashemi, *A Review of the Mechanical Properties of 17-4PH Stainless Steel Produced by Bound Powder Extrusion.* Journal of Manufacturing and Materials Processing, 2023. **7**(5).
75. Soleimani, M., A. Kalhor, and H. Mirzadeh, *Transformation-induced plasticity (TRIP) in advanced steels: A review.* Materials Science and Engineering a-Structural Materials Properties Microstructure and Processing, 2020. **795**.
76. Villa, M., et al., *Aging 17-4 PH martensitic stainless steel prior to hardening: effects on martensitic transformation, microstructure and properties.* Materialia, 2023. **32**.
77. Murayama, M., Y. Katayama, and K. Hono, *Microstructural evolution in a 17-4 PH stainless steel after aging at 400°C.* Metallurgical and Materials Transactions a-Physical Metallurgy and Materials Science, 1999. **30**(2): p. 345-353.
78. Zhao, H., et al., *Automated image mapping and quantification of microstructure heterogeneity in additive manufactured Ti6Al4V.* Materials Characterization, 2019. **147**: p. 131-145.
79. Nezhadfar, P.D., et al., *Improved high cycle fatigue performance of additively manufactured 17-4 PH stainless steel via in-process refining micro-/defect-structure.* Additive Manufacturing, 2020. **36**.